Accepted Manuscript

A 3D finite strain model for intralayer and interlayer crack simulation coupling the phase field approach and cohesive zone model

V. Carollo, J. Reinoso, M. Paggi

A 3D finite strain model for intralayer and interlayer crack simulation coupling the phase field approach and cohesive zone model

V. Carollo[b,*], J. Reinoso[a,b], M. Paggi[b]

[a]*Elasticity and Strength of Materials Group, School of Engineering, Universidad de Sevilla, Camino de los Descubrimientos s/n, 41092, Seville, Spain*
[b]*IMT School for Advanced Studies Lucca, Piazza San Francesco 19, 55100 Lucca, Italy*

Abstract

In this paper, a new 3D finite element formulation which enables simulating the interaction between brittle crack propagation and interface delamination in heterogeneous materials is presented. The Phase Field (PF) model for brittle fracture has been coupled with the Cohesive Zone Model (CZM) within the framework of the large deformation analysis. These numerical techniques have been implemented within a 8-node locking-free solid shell element, relying on the enhanced assumed strain concept, and a 8-node interface finite element, respectively. The predictive capabilities of the proposed formulation have been assessed through the simulation of cracking in flat and curved geometries under in-plane and out-of-plane loadings. The results show the ability of the model to predict complex crack paths where intralayer crack propagation and delamination occur simultaneously and interact. The proposed formulation provides a powerful modelling tool for the simulation of fracture phenomena in heterogeneous materials and laminate structures, which are characterized by the existence of numerous interfaces, such as in photovoltaic laminates.

Keywords: Phase Field, Cohesive Zone Model, Shells, Brittle Fracture, Photovoltaic laminates

1. Introduction

Complex crack patterns such as branching, multiple coalescence and merging are developed in many engineering structures due to the presence of anisotropy and/or heterogeneities, interfaces as well as multiaxial external loadings, among others factors.

As a consequence of its practical importance, modeling crack events in structural components has motivated the development of many computational tools. In this context, discrete crack models which feature cracks as discrete entities are the popular cohesive zone model approach relying on interface finite elements [1, 2], the extended finite element method (XFEM) [3, 4], the embedded finite element method (EFEM) [5, 6, 7]. Though these discrete models have been successfully employed in different applications, they generally lead to arduous efforts for capturing intricate fracture conditions as those described above.

Alternatively, continuum damage models (CDM) use a smeared crack representation over a material band and constitute an easy-solution to be implemented into standard FE codes [8]. Pathological mesh-dependency of CDMs can be alleviated by means of non-local damage methods such as integral-based formulations [9], gradient enhanced models [10, 11, 12, 13, 14], and thick level set methods [15, 16], to quote a few of the existing modeling options.

Rooted on the Griffith's theory of fracture, recent phase field methods can be conceptually categorized as a gradient extended dissipative formulations, which are derived within the context of the so-called *variational approach of fracture* and are especially suitable for brittle materials [17]. In particular, phase field

---

*Corresponding authors
Email address: `valerio.carollo@imtlucca.it` (V. Carollo)

formulations endow a regularization of the Griffith theory using a characteristic length scale l in the spirit of the Γ-convergence [18, 19, 20]. Due to their strong potential to model complex crack patterns, phase field methods have been intensively developed following the landmark thermodynamically consistent formulation proposed by Miehe et al. [21, 22]. Subsequent extensions to dynamic [23, 24] and ductile [25] fracture, higher order approximations [26], multi-field problems [27, 28, 29] and shell structures [30, 31, 32, 33, 34] have been successfully put forward in the last few years.

Recently, further developments of the phase field approach of fracture for heterogeneous media have followed two basic methodologies: (i) the use of a new energy model which combines the brittle energy dissipation due to fracture in the bulk and the interfacial damage, based on the level set method [35, 36], and (ii) the pioneering modeling framework developed in [37], which accounts for the interaction between the phase field model in the bulk and the interface cohesive model. The latter variational concept has shown a great level of accuracy to retrieve linear elastic fracture mechanics (LEFM) results for heterogeneous media, and seminally provided a comprehensive discussion regarding the interaction between both fracture approaches based on the ratio between their characteristic length scales, i.e. l/l_{CZM} where l_{CZM} is the characteristic length scale of the cohesive model.

In this work, we present an extension of the 2D small strain setting developed in [37] for 3D finite strain simulations. Additionally, without loss of generality, the variational formulation for the bulk is particularized to solid shells based on the novel enhanced assumed strain formulation presented in [34] to prevent locking pathologies. Therefore, the proposed formulation enables the interaction of phase field and cohesive zone models for fracture with locking free solid shell elements. Moreover, the present modelling framework could be also integrate alternative shell models [38, 39, 40].

The manuscript is organized as follows. Section 2 outlines the fundamental aspects of the phase field approach of brittle fracture. The variational framework for enhanced assumed strain models for the bulk and the combination of the phase field and the interface cohesive zone model are presented in Section 3. The finite element formulations corresponding to the bulk and the interface are outlined in Section 4. Different numerical examples are investigated in Section 5, showing the performance of the proposed modeling framework. Finally, the main conclusions of the current study are summarized in Section 6. The successful application to a complex fracture problem in Photovoltaic laminates opens a new perspective for the understanding and simulation of mechanical failure modes in photovoltaic modules [41, 42, 43].

2. Phase field approach to fracture

Let $\mathcal{B}_0 \subset \mathbb{R}^3$ the reference configuration of a body, with delimiting boundary $\partial \mathcal{B}_0$, and whose material points are characterized by the position vector $\mathbf{X} \in \mathcal{B}_0$. The current placement of the body at time t is denoted by $\mathcal{B}_t \subset \mathbb{R}^3$ whose boundary is denoted as $\partial \mathcal{B}_t$, being the corresponding position vectors identified by $\mathbf{x} \in \mathcal{B}_t$. The nonlinear deformation map $\boldsymbol{\varphi}(\mathbf{X}, t) : \mathcal{B}_0 \times [0, t] \to \mathbb{R}^3$, where $[0, t]$ is the time step interval, transforms the reference material points ($\mathbf{X} \in \mathcal{B}_0$) onto the corresponding current positions ($\mathbf{x} \in \mathcal{B}_t$): $\mathbf{x} = \boldsymbol{\varphi}(\mathbf{X}, t)$, see Fig. 1. The gradient of the nonlinear deformation map with respect to the reference setting defines the displacement-derived deformation gradient:

$$\mathbf{F}^u := \partial_{\mathbf{X}} \boldsymbol{\varphi}(\mathbf{X}, t) = \nabla_{\mathbf{X}} \boldsymbol{\varphi}(\mathbf{X}, t), \tag{1}$$

which maps the unit reference line elements $d\mathbf{X}$ onto the current line elements $d\mathbf{x} = \mathbf{F}^u d\mathbf{X}$. In the sequel $\nabla_{\mathbf{X}}[\bullet]$ and $\nabla_{\mathbf{x}}[\bullet]$ respectively identify the Lagrangian and Eulerian gradient operators. The Jacobian of the transformation is restricted by the condition $J^u := \det[\mathbf{F}^u] > 0$, where $\det[\bullet]$ stands for the determinant operator.

We also equip the Lagrangian and Eulerian manifolds with the covariant reference and current metric tensors $\mathbf{G}$ and $\mathbf{g}$, respectively. Correspondingly, the displacement-derived left $\mathbf{C}^u$ and right $\mathbf{b}^u$ Cauchy-Green deformation tensors read

$$\mathbf{C}^u = [\mathbf{F}^u]^{\mathrm{T}} \mathbf{g}[\mathbf{F}^u], \quad \mathbf{b}^u = [\mathbf{F}^u] \mathbf{G}^{-1} [\mathbf{F}^u]^{\mathrm{T}}. \tag{2}$$

Then, the displacement-derived Green-Lagrange $\mathbf{E}^u$ and Euler-Almansi $\boldsymbol{\varepsilon}^u$ strain tensors are defined as

$$\mathbf{E}^u := \frac{1}{2} [\mathbf{C}^u - \mathbf{G}], \quad \boldsymbol{\varepsilon}^u := \frac{1}{2} [\mathbf{g} - [\mathbf{b}^u]^{-1}]. \tag{3}$$
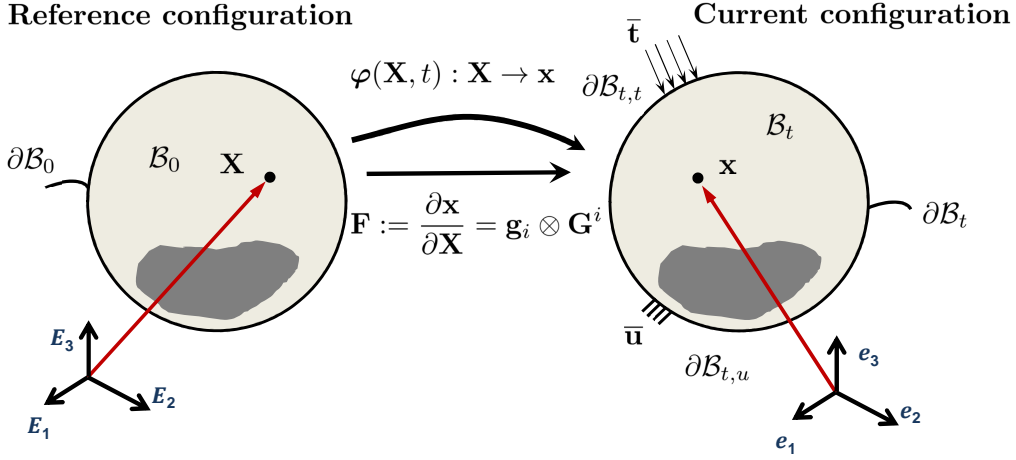
2

Figure 1: Nonlinear deformation of the solid. Definition of reference $\mathcal{B}_0$ and current $\mathcal{B}_t$ configurations of the solid. The nonlinear deformation map is defined as $\boldsymbol{\varphi}(\mathbf{X}, t) : \mathcal{B}_0 \times [0, t] \rightarrow \mathbb{R}^3$, where $[0, t]$ is the time step interval, and the deformation gradient reads $\mathbf{F}^u : \nabla_{\mathbf{X}} \boldsymbol{\varphi}(\mathbf{X}, t)$. The solid is subjected to prescribed static $\bar{\mathbf{t}}$ on $\partial \mathcal{B}_{t,t}$ and kinematic actions $\bar{\mathbf{u}}$ on $\partial \mathcal{B}_{t,u}$.

Additionally, in the presence of fracture, we define the crack phase field variable $\mathfrak{d} : \mathcal{B}_0 \times [0, t] \rightarrow [0, 1]$, which allows the identification of intact $\mathfrak{d}(\mathbf{X}, t) = 0$ and broken $\mathfrak{d}(\mathbf{X}, t) = 1$ states at $\mathbf{X} \in \mathcal{B}_0$, see Fig. 2. Given crack surface topology at time t as $\Gamma_c(t) \subset \mathbb{R}^2$ in the solid $\mathcal{B}_0$, the regularized crack functional adopts the form

$$\Gamma_c(\mathfrak{d}) := \int_{\mathcal{B}_0} \gamma(\mathfrak{d}, \nabla_{\mathbf{X}} \mathfrak{d}) \, d\Omega, \tag{4}$$

with

$$\gamma(\mathfrak{d}, \nabla_{\mathbf{X}} \mathfrak{d}) = \frac{1}{2l} \mathfrak{d}^2 + \frac{l}{2} |\nabla_{\mathbf{X}} \mathfrak{d}|^2. \tag{5}$$

In line with [21, 22], the minimization problem associated with the diffusive crack topology reads

$$\mathfrak{d}(\mathbf{X}, t) = \text{Arg}\{ \inf_{\mathfrak{d} \in \mathcal{W}_{\Gamma(t)}} \Gamma_c(\mathfrak{d}) \} \tag{6}$$

subject to the Dirichlet-type constraint: $\mathcal{W}_{\Gamma(t)} = \{\mathfrak{d} \,|\, \mathfrak{d}(\mathbf{X}, t) = 1 \text{ at } \mathbf{X} \in \Gamma_c(t)\}$. Therefore, the Euler–Lagrange equations of the previous variational principle are given by

$$\mathfrak{d} - l^2 \Delta \mathfrak{d} = 0 \quad \text{in } \mathcal{B}_0 \quad \text{and} \quad \nabla_{\mathbf{X}} \mathfrak{d} \cdot \mathbf{n} = 0 \quad \text{on } \partial \mathcal{B}_0 \tag{7}$$

where $\Delta \mathfrak{d}$ is the Laplacian of the crack phase field variable with respect to the reference setting, and $\mathbf{n}$ identifies the outer normal vector on $\partial \mathcal{B}_0$.

3. Computational framework

In this section, we derive the continuous framework and the 3D interface formulation compatible with the phase field approach to fracture in the bulk for nonlinear applications. The current method is especially suitable for heterogeneous media and structures with the presence of interfaces, which can occur in many engineering applications such as composite laminates [44, 35], battery systems, modern electronic devices, among many others.

The fundamental idea of the proposed framework is based on the consideration of a 3D arbitrary system which includes the existence of an interface Γ_i and a crack within the bulk domain Γ_c, see Fig 3.a.
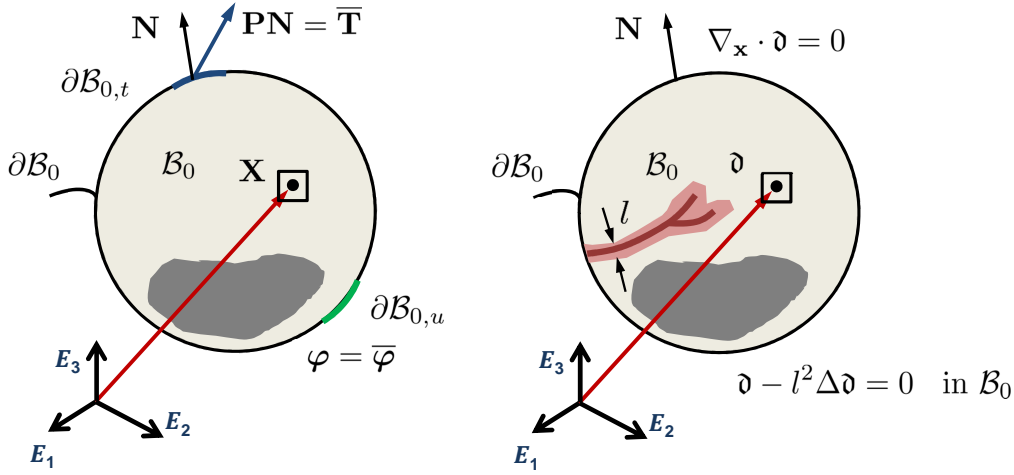
3

Figure 2: The multi-field problem for cracked bodies based on the phase field approach of fracture. Left: Mechanical problem. Right: Crack phase field problem.

Consequently, in this scenario, two dissipative mechanisms can concurrently evolve and release the corresponding fracture energies. To clarify the notation, the reference and current position vectors at the flanks of the cohesive interface are respectively denoted as $\mathbf{X}_i$ and $\mathbf{x}_i$, whereas the corresponding vectors along the midsurface of the cohesive interface are given by $\overline{\mathbf{X}}_i$ and $\overline{\mathbf{x}}_i$.

In the sequel, we comprehensively present the fundamental aspects of the computational framework under development. After introducing the variational basis of the coupled problem in Section 3.1, we address the variational formalism of the phase field approach to brittle fracture in the bulk in Section 3.2. We specialize the proposed formulation for enhanced assumed strain (EAS) solid shells in order to alleviate locking pathologies. In particular, we adopt the additive decomposition of the Green-Lagrange strain tensor $\mathbf{E} = \mathbf{E}^u + \tilde{\mathbf{E}}$, where $\mathbf{E}^u$ and $\tilde{\mathbf{E}}$ denote the compatible and the incompatible counterparts [45, 46], respectively. Nevertheless, it is worth mentioning that any other kind of element topology can be integrated into the current formulation in a straightforward manner. Subsequently, in Section 3.3, the variational formulation of the interface model is derived. Finally, the constitutive behavior of the developed interface for 3D applications including geometric nonlinear effects is outlined in Section 3.4.

3.1. Variational basis for coupled phase field approach to fracture in the bulk and cohesive interface delamination

Inspired by [34], we construct the variational formulation through the Hu-Washizu variational principle, where the displacements $\mathbf{u}$, the incompatible strains $\tilde{\mathbf{E}}$, the second Piola-Kirchhoff stress tensor $\mathbf{S}$, and the crack phase field variable $\mathfrak{d}$ constitute the independent fields of the formulation. According to the Griffith's theory of brittle fracture, for cracked bodies, this variational formalism in the reference configuration can be expressed as

$$\Pi(\mathbf{u}, \tilde{\mathbf{E}}, \mathbf{S}, \mathfrak{d}) = \underbrace{\int_{\mathcal{B}_0 \backslash \Gamma} \mathfrak{g}(\mathfrak{d}) \Psi(\mathbf{E}) \, \mathrm{d}\Omega - \int_{\mathcal{B}_0} \mathbf{S} : \tilde{\mathbf{E}} \, \mathrm{d}\Omega}_{\Pi_{\text{int}}^b} + \underbrace{\int_{\Gamma} \mathcal{G}_c \, \mathrm{d}\Gamma}_{\Pi_{\text{fr}}} + \Pi_{\text{ext}}, \tag{8}$$

where the internal contribution of the bulk is denoted by Π_{int}^b, whilst Π_{fr} identifies the dissipative contribution due to fracture events; furthermore, the prescribed external surface and body actions are arranged in the term Π_{ext}. In Eq.(8), $\Psi(\mathbf{E})$ is the effective Helmholtz free-energy function in the bulk for undamaged hyperelastic materials and $\mathfrak{g}(\mathfrak{d})$ is the degradation function, which satisfies $\mathfrak{g}(0)\Psi(\mathbf{E}) = \Psi(\mathbf{E})$ for undamaged states, and $\mathfrak{g}(1)\Psi(\mathbf{E}) = \mathcal{K}\Psi(\mathbf{E})$ for fully damaged states, being $\mathcal{K} \approx 0$ is a residual positive parameter that

4

prevents numerical instabilities [47]. Thus, without loss of generality, we adopt as degradation function $\mathfrak{g}(\mathfrak{d}) = [1 - \mathfrak{d}]^2 + \mathcal{K}$. Moreover, it is worth mentioning that the second integral term of Π_{int}^b accounts for the contribution of the second Piola-Kirchhoff stress tensor over the incompatible strains in the view of the EAS method.

Referring to the dissipative term in Eq.(8), we advocate the fundamental hypothesis put forward in [48] stating that such term can be additively decomposed into two contributions [37]: (i) the dissipated energy due to the fracture in the bulk Π_{fr}^b that is governed by the phase field approach to brittle fracture, and (ii) the energy dissipation that takes place at the existing interface Π_{fr}^i. Introducing such a decomposition into Eq.(8), a modified Hu-Washizu variational principle can be recast as

$$\Pi(\mathbf{u}, \tilde{\mathbf{E}}, \mathbf{S}, \mathfrak{d}) = \int_{\mathcal{B}_0 \backslash \Gamma} \mathfrak{g}(\mathfrak{d}) \Psi(\mathbf{E}) \, \mathrm{d}\Omega - \int_{\mathcal{B}_0} \mathbf{S} : \tilde{\mathbf{E}} \, \mathrm{d}\Omega + \underbrace{\int_{\mathcal{B}_0} \mathcal{G}_c^b \gamma(\mathfrak{d}, \nabla_{\mathbf{X}} \mathfrak{d}) \, \mathrm{d}\Omega}_{\Pi_{\text{fr}}^b} + \underbrace{\int_{\Gamma_i} \mathcal{G}_c^i(\mathbf{u}, \mathfrak{d}) \, \mathrm{d}\Gamma}_{\Pi_{\text{fr}}^i} + \Pi_{\text{ext}}, \quad (9)$$

where $\mathcal{G}_c^b$ identifies the dissipated energy in the bulk according to the Griffith's theory [49], whereas $\mathcal{G}_c^i(\mathbf{u}, \mathfrak{d})$ stands for the fracture energy dissipated at the interface based on the cohesive zone model.

Relying on the previous derivations, the final form of the variational formulation can be split into the bulk $\Pi^b(\mathbf{S}, \tilde{\mathbf{E}}, \mathbf{u}, \mathfrak{d})$ and interface contributions $\Pi^i(\mathbf{u}, \mathfrak{d})$ as follows

$$\Pi(\mathbf{u}, \tilde{\mathbf{E}}, \mathbf{S}, \mathfrak{d}) = \Pi^b(\mathbf{S}, \tilde{\mathbf{E}}, \mathbf{u}, \mathfrak{d}) + \Pi^i(\mathbf{u}, \mathfrak{d}) \quad (10)$$

with

$$\Pi^b(\mathbf{u}, \tilde{\mathbf{E}}, \mathbf{S}, \mathfrak{d}) = \int_{\mathcal{B}_0 \backslash \Gamma} \mathfrak{g}(\mathfrak{d}) \Psi(\mathbf{E}) \, \mathrm{d}\Omega - \int_{\mathcal{B}_0} \mathbf{S} : \tilde{\mathbf{E}} \, \mathrm{d}\Omega + \int_{\mathcal{B}_0} \mathcal{G}_c^b \gamma(\mathfrak{d}, \nabla_{\mathbf{X}} \mathfrak{d}) \, \mathrm{d}\Omega + \Pi_{\text{ext}} \quad (11)$$

$$\Pi^i(\mathbf{u}, \mathfrak{d}) = \int_{\Gamma_i} \mathcal{G}_c^i(\mathbf{u}, \mathfrak{d}) \, \mathrm{d}\Gamma. \quad (12)$$

Note that the fracture energy at the interface depends on the displacement field (as standard zone cohesive models) and the crack phase field variable in the bulk surrounding the interface crack, which governs the apparent stiffness of the cohesive model as described in Section 3.4.

3.2. Variational formulation of the boundary value problem at the bulk: the enhanced assumed strain method for cracked solids

Focusing the attention on the bulk contribution presented in Section 3.1, we construct the corresponding weak form by means of performing the first variation of the functional given in Eq. (11) through directional derivative concept with respect to the four independent fields. This leads to the following residual equations:

$$\mathcal{R}^u(\mathbf{u}, \delta\mathbf{u}, \tilde{\mathbf{E}}, \mathbf{S}, \mathfrak{d}) = \mathcal{R}_{\text{int}}^u - \mathcal{R}_{\text{ext}}^u = \int_{\mathcal{B}_0} \mathfrak{g}(\mathfrak{d}) \frac{\partial \Psi}{\partial \mathbf{E}} : \delta\mathbf{E}^u \, \mathrm{d}\Omega + \delta\Pi_{\text{ext}}(\mathbf{u}) = 0, \quad \forall \delta\mathbf{u} \in \mathfrak{V}^u, \quad (13)$$

$$\mathcal{R}^{\tilde{E}}(\mathbf{u}, \tilde{\mathbf{E}}, \delta\tilde{\mathbf{E}}, \mathbf{S}, \mathfrak{d}) = \int_{\mathcal{B}_0} \mathfrak{g}(\mathfrak{d}) \frac{\partial \Psi}{\partial \mathbf{E}} : \delta\tilde{\mathbf{E}} \, \mathrm{d}\Omega - \int_{\mathcal{B}_0} \mathbf{S} : \delta\tilde{\mathbf{E}} \, \mathrm{d}\Omega = 0, \quad \forall \delta\tilde{\mathbf{E}} \in \mathfrak{V}^{\tilde{E}}, \quad (14)$$

$$\mathcal{R}^S(\mathbf{u}, \tilde{\mathbf{E}}, \mathbf{S}, \delta\mathbf{S}, \mathfrak{d}) = \int_{\mathcal{B}_0} \delta\mathbf{S} : \tilde{\mathbf{E}} \, \mathrm{d}\Omega = 0, \quad \forall \delta\mathbf{S} \in \mathfrak{V}^S, \quad (15)$$

$$\mathcal{R}^{\mathfrak{d}}(\mathbf{u}, \tilde{\mathbf{E}}, \mathbf{S}, \mathfrak{d}, \delta\mathfrak{d}) = \int_{\mathcal{B}_0} -2(1 - \mathfrak{d})\delta\mathfrak{d}\Psi(\mathbf{E}) \, \mathrm{d}\Omega + \int_{\mathcal{B}_0} \mathcal{G}_c^b l \left[\frac{1}{l^2} \mathfrak{d}\delta\mathfrak{d} + \nabla_{\mathbf{X}} \mathfrak{d} \cdot \nabla_{\mathbf{X}}(\delta\mathfrak{d}) \right] \mathrm{d}\Omega = 0, \quad \forall \delta\mathfrak{d} \in \mathfrak{V}^{\mathfrak{d}}, \quad (16)$$

where $\mathfrak{V}^u = \left\{ \delta\mathbf{u} \in [H^1(\mathcal{B}_0)] : \delta\mathbf{u} = \mathbf{0} \text{ on } \partial\mathcal{B}_{0,u} \right\}$ identifies the space of admissible displacement variations; $\mathfrak{V}^{\tilde{E}} = [L_2(\mathcal{B}_0)]$ and $\mathfrak{V}^S = [L_2(\mathcal{B}_0)]$ identify the admissible spaces corresponding to the test functions of the incompatible strain and the stress fields, respectively; and finally $\mathfrak{V}^{\mathfrak{d}} = \left\{ \delta\mathfrak{d} \in \mathcal{H}^1(\mathcal{B}_0) \,|\, \delta\mathfrak{d} = 0 \text{ on } \Gamma_c \right\}$ is the space of admissible test functions for the crack phase field variable.
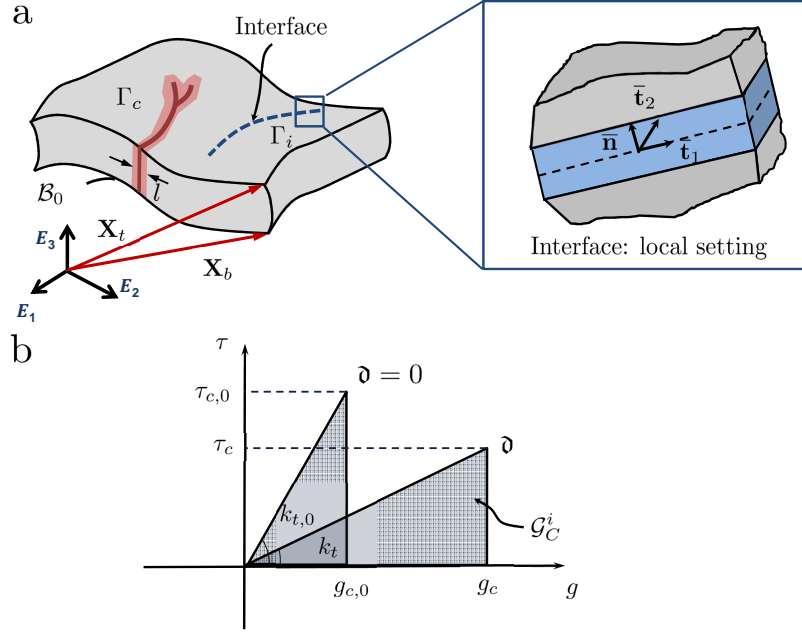
5

Figure 3: (a) Thin-walled structure with the presence of a crack within the bulk Γ_c and a prescribed interface Γ_i. (b) Constitutive interface cohesive formulation based on a tension cut-off model for a generic fracture mode including the variation of the interface stiffness with the crack phase field variable of the surrounding body ($\tau_{c,0}$ and τ_c identify the generic traction component and its critical value at the interface, respectively, $g_{c,0}$ and g_c denote the relative displacement at the interface for $\mathfrak{d} = 0$ and a generic $\mathfrak{d}$, respectively, and finally $k_{t,0}$ and k_t stand for the interface stiffness for the two above configuration one.

Recalling the orthogonality condition for the stress field $\mathbf{S}$ and the enhanced strain field $\tilde{\mathbf{E}}$ [50], the weak form of the boundary value problem associated with the cracked bulk is reduced to the following three field problem

$$\mathcal{R}^u(\mathbf{u}, \delta\mathbf{u}, \tilde{\mathbf{E}}, \mathfrak{d}) = \mathcal{R}^u_{\text{int}} - \mathcal{R}^u_{\text{ext}} = \int_{\mathcal{B}_0} \mathfrak{g}(\mathfrak{d}) \frac{\partial \Psi}{\partial \mathbf{E}} : \delta\mathbf{E}^u \, d\Omega + \delta\Pi_{\text{ext}}(\mathbf{u}) = 0, \tag{17}$$

$$\mathcal{R}^{\tilde{E}}(\mathbf{u}, \tilde{\mathbf{E}}, \delta\tilde{\mathbf{E}}, \mathfrak{d}) = \int_{\mathcal{B}_0} \mathfrak{g}(\mathfrak{d}) \frac{\partial \Psi}{\partial \mathbf{E}} : \delta\tilde{\mathbf{E}} \, d\Omega = 0, \tag{18}$$

$$\mathcal{R}^{\mathfrak{d}}(\mathbf{u}, \tilde{\mathbf{E}}, \mathfrak{d}, \delta\mathfrak{d}) = \int_{\mathcal{B}_0} -2(1-\mathfrak{d})\delta\mathfrak{d}\Psi(\mathbf{E}) \, d\Omega + \int_{\mathcal{B}_0} \mathcal{G}^b_c l \left[\frac{1}{l^2}\mathfrak{d}\delta\mathfrak{d} + \nabla_{\mathbf{X}}\mathfrak{d} \cdot \nabla_{\mathbf{X}}(\delta\mathfrak{d}) \right] d\Omega = 0. \tag{19}$$

The nonlinear system given in Eqs.(17)-(19) is solved by means of the standard incremental-iterative Newton-Raphson method. For this purpose, the consistent linearization of these equations can be expressed as

$$\hat{L}[\mathcal{R}^u(\mathbf{u}, \delta\mathbf{u}, \tilde{\mathbf{E}}, \mathfrak{d})] \cdot [\Delta\mathbf{u}, \Delta\tilde{\mathbf{E}}, \Delta\mathfrak{d}] = \int_{\mathcal{B}_0} \mathfrak{g}(\mathfrak{d}) \left[\delta\mathbf{E}^u : \frac{\partial^2 \Psi}{\partial \mathbf{E}^2} : \Delta\mathbf{E}^u + \frac{\partial \Psi}{\partial \mathbf{E}} : \Delta\delta\mathbf{E}^u \right] d\Omega +$$

$$\int_{\mathcal{B}_0} \mathfrak{g}(\mathfrak{d}) \left[\delta\mathbf{E}^u : \frac{\partial^2 \Psi}{\partial \mathbf{E}^2} : \Delta\tilde{\mathbf{E}} \right] d\Omega \int_{\mathcal{B}_0} \delta\mathbf{E}^u : \frac{\partial \Psi}{\partial \mathbf{E}} \frac{\partial \mathfrak{g}(\mathfrak{d})}{\partial \mathfrak{d}} \Delta\mathfrak{d} \, d\Omega, \tag{20}$$

$$\hat{L}[\mathcal{R}^{\tilde{E}}(\mathbf{u}, \tilde{\mathbf{E}}, \delta\tilde{\mathbf{E}}, \mathfrak{d})] \cdot [\Delta\mathbf{u}, \Delta\tilde{\mathbf{E}}, \Delta\mathfrak{d}] = \int_{\mathcal{B}_0} \mathfrak{g}(\mathfrak{d}) \left[\delta\tilde{\mathbf{E}} : \frac{\partial^2 \Psi}{\partial \mathbf{E}^2} : \Delta\mathbf{E}^u + \delta\tilde{\mathbf{E}} : \frac{\partial^2 \Psi}{\partial \mathbf{E}^2} : \Delta\tilde{\mathbf{E}} \right] d\Omega +$$

$$\int_{\mathcal{B}_0} \delta\tilde{\mathbf{E}} : \frac{\partial \Psi}{\partial \mathbf{E}} \frac{\partial \mathfrak{g}(\mathfrak{d})}{\partial \mathfrak{d}} \Delta\mathfrak{d} \, d\Omega, \tag{21}$$

6

$$\hat{L}[\mathcal{R}^{\mathfrak{d}}(\mathbf{u}, \tilde{\mathbf{E}}, \mathfrak{d}, \delta\mathfrak{d})] \cdot [\Delta\mathbf{u}, \Delta\tilde{\mathbf{E}}, \Delta\mathfrak{d}] = \int_{\mathcal{B}_0} -2(1-\mathfrak{d})\delta\mathfrak{d}\frac{\partial\Psi}{\partial\mathbf{E}} : \Delta\mathbf{E}^u \, d\Omega + \int_{\mathcal{B}_0} -2(1-\mathfrak{d})\delta\mathfrak{d}\frac{\partial\Psi}{\partial\mathbf{E}} : \Delta\tilde{\mathbf{E}} \, d\Omega$$

$$\int_{\mathcal{B}_0} 2\delta\mathfrak{d}\Psi(\mathbf{E})\Delta\mathfrak{d} \, d\Omega + \int_{\mathcal{B}_0} \mathcal{G}_c^b l \left[\frac{1}{l^2}\delta\mathfrak{d}\Delta\mathfrak{d} + \nabla_{\mathbf{X}}\Delta\mathfrak{d} \cdot \nabla_{\mathbf{X}}(\delta\mathfrak{d})\right] d\Omega. \tag{22}$$

The first variation of the displacement-derived Green–Lagrange strain tensor takes the form

$$\delta\mathbf{E}^u = \frac{1}{2}\left[\delta\mathbf{g}_i \cdot \mathbf{g}_j + \mathbf{g}_i \cdot \delta\mathbf{g}_j\right]\mathbf{G}^i \otimes \mathbf{G}^j, \tag{23}$$

whereas its linearized virtual displacement-derived Green–Lagrange strain tensor in the convective setting reads

$$\Delta\delta\mathbf{E}^u = \frac{1}{2}\left[\delta\mathbf{g}_i \cdot \Delta\mathbf{g}_j + \Delta\mathbf{g}_i \cdot \delta\mathbf{g}_j\right]\mathbf{G}^i \otimes \mathbf{G}^j. \tag{24}$$

The previous derivation leads to a fully coupled system of equation, which is solved according to a monolithic solution scheme as is discussed in Section 4.1 [34].

Regarding the material formulation, a hyperelastic neo-Hookean isotropic constitutive response is assumed for the numerical implementation of the current framework, with:

$$\Psi(\mathbf{C}) = \frac{\lambda}{2}\left(\ln J\right)^2 - \mu\ln J + \frac{\mu}{2}\left(\text{tr}[\mathbf{C}] - 3\right), \tag{25a}$$

$$\mathbf{S}(\mathbf{C}) = 2\partial_{\mathbf{C}}\Psi(\mathbf{C}) = \left(\lambda\ln J - \mu\right)\mathbf{C}^{-1} + \mu\mathbb{I}_2, \tag{25b}$$

$$\mathbb{C}(\mathbf{C}) = 4\partial_{\mathbf{CC}}\Psi(\mathbf{C}) = \lambda\mathbf{C}^{-1} \otimes \mathbf{C}^{-1} + 2\left(\lambda\ln J - \mu\right)\frac{\partial\mathbf{C}^{-1}}{\partial\mathbf{C}}, \tag{25c}$$

where J identifies the determinant of the deformation gradient $\mathbf{F}$ accounting for the consideration of the incompatible strains [34].

Finally, standard Dirichlet- and Neumann-type boundary conditions are considered for the boundary value problem in the bulk.

3.3. Variational formulation of the interface contribution

The point of departure of the weak form of the interface contribution is the term Π_{fr}^i in Eq.(9). In the following, we refer to the derivation of the displacement field $\mathbf{u}_i$ and the crack phase field $\mathfrak{d}_i$, which are associated with the two flanks of the interface. Correspondingly, the local displacement gap vector on the midsurface of the interface $\mathbf{g}_{\text{loc}}$ can be computed by means of a suitable difference operator $\mathbf{L}$ [37], and a rotation operator $\mathbf{R}(\mathbf{u}_i)$:

$$\mathbf{g}_{\text{loc}} = \mathbf{R}(\mathbf{u}_i)\mathbf{L}\mathbf{u}_i \tag{26}$$

The previous transformation is required due to the fact that most of the interface formulations employ a local setting to trigger the relative gaps between the two flanks to distinguish fracture Modes for nonlinear constitutive models [51, 52]. The variation $\delta\mathbf{g}_{\text{loc}}$ and the increment $\Delta\mathbf{g}_{\text{loc}}$ of the local gap vector render

$$\delta\mathbf{g}_{\text{loc}} = \left[\frac{\partial\mathbf{R}(\mathbf{u}_i)}{\partial\mathbf{u}_i}\mathbf{L}\mathbf{u}_i + \mathbf{R}(\mathbf{u}_i)\mathbf{L}\right]\delta\mathbf{u}_i; \quad \Delta\mathbf{g}_{\text{loc}} = \left[\frac{\partial\mathbf{R}(\mathbf{u}_i)}{\partial\mathbf{u}_i}\mathbf{L}\mathbf{u}_i + \mathbf{R}(\mathbf{u}_i)\mathbf{L}\right]\Delta\mathbf{u}_i \tag{27}$$

Note that an additional geometric term stems from the linearized virtual local gap $\Delta\delta\mathbf{g}_{\text{loc}}$:

$$\Delta\delta\mathbf{g}_{\text{loc}} = \left[\frac{\partial^2\mathbf{R}(\mathbf{u}_i)}{\partial\mathbf{u}_i^2}\mathbf{L}\mathbf{u}_i\delta\mathbf{u}_i + 2\frac{\partial\mathbf{R}(\mathbf{u}_i)}{\partial\mathbf{u}_i}\mathbf{L}\delta\mathbf{u}_i\right]\Delta\mathbf{u}_i \approx \left[2\frac{\partial\mathbf{R}(\mathbf{u}_i)}{\partial\mathbf{u}_i}\mathbf{L}\delta\mathbf{u}_i\right]\Delta\mathbf{u}_i \tag{28}$$

As addressed in [53], to simplify the current interface model, the second derivative of the rotation matrix with respect to the displacement field can be neglected due to its minor representativeness. Moreover, the derivative of the Jacobian, which defines the measure of the element length, will also be neglected due to its minor contribution, as rigorously shown in [54].

7

The crack phase field is averaged along the midsurface between the two flanks as follows: $\hat{\mathfrak{d}}_i = \mathbf{L}\mathfrak{d}_i$. The, the corresponding variation $\delta\hat{\mathfrak{d}}_i$ and increment of the averaged crack phase field variable at the interface reads

$$\delta\hat{\mathfrak{d}}_i = \mathbf{M}\delta\mathfrak{d}_i; \quad \Delta\hat{\mathfrak{d}}_i = \mathbf{M}\Delta\mathfrak{d}_i \tag{29}$$

Based on Eq.(12), the first variation of with respect to the two independent fields yields the following residual equations

$$\mathcal{R}^{\overline{u}_i}(\mathbf{u}_i, \delta\mathbf{u}_i, \hat{\mathfrak{d}}_i) = \int_{\Gamma_i} [\delta\mathbf{g}_{\mathrm{loc}}]^{\mathrm{T}} \left[\frac{\partial \mathcal{G}_c^i}{\partial \mathbf{g}_{\mathrm{loc}}}\right] \mathrm{d}\Gamma, \tag{30}$$

$$\mathcal{R}^{\hat{\mathfrak{d}}_i}(\mathbf{u}_i, \hat{\mathfrak{d}}_i, \delta\hat{\mathfrak{d}}_i) = \int_{\Gamma_i} \left[\delta\hat{\mathfrak{d}}_i\right]^{\mathrm{T}} \left[\frac{\partial \mathcal{G}_c^i}{\partial \hat{\mathfrak{d}}_i}\right] \mathrm{d}\Gamma. \tag{31}$$

The consistent linearization of the residual forms given in Eqs.(30)–(31) yields

$$\hat{L}[\mathcal{R}^{\overline{u}_i}(\mathbf{u}_i, \delta\mathbf{u}_i, \hat{\mathfrak{d}}_i)] \cdot [\Delta\mathbf{u}_i, \Delta\hat{\mathfrak{d}}_i] = \int_{\Gamma_i} [\Delta\delta\mathbf{g}_{\mathrm{loc}}]^{\mathrm{T}} \left[\frac{\partial \mathcal{G}_c^i}{\partial \mathbf{g}_{\mathrm{loc}}}\right] \mathrm{d}\Gamma + [\delta\mathbf{g}_{\mathrm{loc}}]^{\mathrm{T}} \left[\frac{\partial^2 \mathcal{G}_c^i}{\partial \mathbf{g}_{\mathrm{loc}}^2}\right] \Delta\mathbf{g}_{\mathrm{loc}} \, \mathrm{d}\Gamma +$$

$$\int_{\Gamma_i} [\delta\mathbf{g}_{\mathrm{loc}}]^{\mathrm{T}} \left[\frac{\partial^2 \mathcal{G}_c^i}{\partial \mathbf{g}_{\mathrm{loc}} \partial \hat{\mathfrak{d}}_i}\right] \Delta\hat{\mathfrak{d}}_i \, \mathrm{d}\Gamma, \tag{32}$$

$$\hat{L}[\mathcal{R}^{\hat{\mathfrak{d}}_i}(\mathbf{u}_i, \hat{\mathfrak{d}}_i, \delta\hat{\mathfrak{d}}_i)] \cdot [\Delta\mathbf{u}_i, \Delta\hat{\mathfrak{d}}_i] \int_{\Gamma_i} \left[\delta\hat{\mathfrak{d}}_i\right]^{\mathrm{T}} \left[\frac{\partial^2 \mathcal{G}_c^i}{\partial \hat{\mathfrak{d}}_i^2}\right] \Delta\hat{\mathfrak{d}}_i \, \mathrm{d}\Gamma + \int_{\Gamma_i} \left[\delta\hat{\mathfrak{d}}_i\right]^{\mathrm{T}} \left[\frac{\partial^2 \mathcal{G}_c^i}{\partial \hat{\mathfrak{d}}_i \partial \mathbf{g}_{\mathrm{loc}}}\right] \Delta\mathbf{u}_i \, \mathrm{d}\Gamma. \tag{33}$$

The geometrical effects arise from the variation of the rotation operator with respect to the displacement field [55, 53]. The proposed model represents a generalization of the 2D formulation for small displacements in [37] to 3D applications and finite deformations.

3.4. Interface constitutive formulation

The postulation of the current 3D interface formulation relies on the assumption that the energy release due to fracture is given by the sum of the energy release due to Modes I, II and III fracture. In particular, we adopt a tension cut-off interface model upon failure for each individual fracture Mode. This model is a Linear Elastic Interface Model (LEBIM) and can be idealized as a continuous distribution of linear springs along the interface, see [56, 57]. This interface formulation features for each fracture mode a linear response, characterized by its given stiffness, which can be set proportional to the ratio between the Young modulus of the interface and its thickness for adhesive layers.

The constitutive response for fracture Mode I (see Fig. 3.b for a generic fracture Mode) reads

$$S_n = \begin{cases} k_n \dfrac{g_n}{g_{nc}}, & \text{if } 0 < \dfrac{g_n}{g_{nc}} < 1; \\ 0, & \text{if } \dfrac{g_n}{g_{nc}} \geq 1, \end{cases} \tag{34}$$

where S_n identifies the normal Piola traction component of the interface, being S_c its corresponding critical value; k_n is the interface stiffness, whereas g_n and g_{nc} are the normal displacement gap and its critical value in the local setting of the interface. Note that the previous cohesive law is further equipped by a penalty formulation in compression with the aim of precluding the inter-penetration of the corresponding flanks.

The interface response given in Eq.(34) is further extended for fracture Modes II and III, which obey the following relationships

$$S_{t1} = \begin{cases} k_{t1} \dfrac{g_{t1}}{g_{t1c}}, & \text{if } 0 < \dfrac{g_{t1}}{g_{t1c}} < 1; \\ 0, & \text{if } \dfrac{g_{t1}}{g_{t1c}} \geq 1, \end{cases} \qquad S_{t2} = \begin{cases} k_{t2} \dfrac{g_{t2}}{g_{t2c}}, & \text{if } 0 < \dfrac{g_{t2}}{g_{t2c}} < 1; \\ 0, & \text{if } \dfrac{g_{t2}}{g_{t2c}} \geq 1, \end{cases} \tag{35}$$

8

In Eq.(35), S_{t1} and S_{t2} stand for the tangential Piola traction components associated with the fracture Modes II and III, respectively, whose corresponding critical values are denoted as S_{t1c} and S_{t2c}. The interface stiffness properties for fracture Modes II and III are given by k_{t1} and k_{t2}, respectively. Moreover, g_{t1} and g_{t1c} are the tangential displacement gap and its critical value for fracture Mode II, whilst g_{t2} and g_{t2c} stand for the same quantities for fracture Mode III.

Relying on the previous considerations, the fracture energies for Modes I, II and III render

$$\mathcal{G}_{IC}^i = \frac{1}{2}S_n g_{nc} = \frac{1}{2}k_n g_{nc}^2; \quad \mathcal{G}_{IIC}^i = \frac{1}{2}S_{t1} g_{t1c} = \frac{1}{2}k_{t1} g_{t1c}^2; \quad \mathcal{G}_{IIIC}^i = \frac{1}{2}S_{t2} g_{t2c} = \frac{1}{2}k_{t2} g_{t2c}^2. \tag{36}$$

In order to make the interface formulation dependent of the crack phase field variable of the surrounding bulk, we recall that the critical openings triggering the interface failure are function of $\hat{\mathfrak{d}}_i$ but keeping constant the critical energy release rate for each fracture Mode. In particular, we consider that the critical gap at the interfaces increases as the crack phase field variable of the adjoining bulk evolves from 0 to 1. Thus, the following relationship to express the dependency of the critical gaps upon $\hat{\mathfrak{d}}_i$ can be proposed:

$$g_{ic}(\mathfrak{d}_i) = (1 - \mathfrak{d}_i)g_{ic,0} + \mathfrak{d}_i g_{ic,1}, \quad \text{with } i = n, t1, t2. \tag{37}$$

In Eq.(37), $g_{ic,0}$ and $g_{ic,1}$ denote the critical gaps for the states corresponding to undamaged ($\mathfrak{d}_i = 0$) and fully damaged ($\mathfrak{d}_i = 1$) surrounding bulk. Through the imposition that the fracture energies for each Mode is independent of the crack phase field value, a closed-form expression for the interface stiffnesses can be obtained by equating the fracture energies for an arbitrary value of $\mathfrak{d}_i$ and for $\mathfrak{d}_i = 0$:

$$k_n = k_{n,0}\left(\frac{g_{nc,0}}{g_{nc}}\right)^2, \quad k_{t1} = k_{t1,0}\left(\frac{g_{t1c,0}}{g_{t1c}}\right)^2, \quad k_{t2} = k_{t2,0}\left(\frac{g_{t2c,0}}{g_{t2c}}\right)^2, \tag{38}$$

where $k_{n,0}$, $k_{t1,0}$ and $k_{t2,0}$ are the interface stiffness for intact surrounding bulk ($\hat{\mathfrak{d}}_i = 0$) for the fracture Modes I, II and III, respectively, whilst their corresponding values for a generic damage state in the bulk $\mathfrak{d}_i$ are denoted by k_n, k_{t1} and k_{t2}.

Therefore, the following closed-form expressions for the Modes I, II and III energy release rates can be derived:

$$\mathcal{G}_I^i(\mathfrak{d}_i) = \frac{1}{2}k_{n,0} g_n^2 \frac{g_{nc,0}^2}{\left[(1 - \mathfrak{d}_i)g_{nc,0} + \mathfrak{d}_i g_{nc,1}\right]^2}, \tag{39}$$

$$\mathcal{G}_{II}^i(\mathfrak{d}_i) = \frac{1}{2}k_{t1,0} g_t^2 \frac{g_{t1c,0}^2}{\left[(1 - \mathfrak{d}_i)g_{t1c,0} + \mathfrak{d}_i g_{t1c,1}\right]^2}, \tag{40}$$

$$\mathcal{G}_{III}^i(\mathfrak{d}_i) = \frac{1}{2}k_{t2,0} g_{t2}^2 \frac{g_{t2c,0}^2}{\left[(1 - \mathfrak{d}_i)g_{t2c,0} + \mathfrak{d}_i g_{t2c,1}\right]^2}. \tag{41}$$

Without loss of generality, a standard quadratic criterion to trigger the interface failure under Mixed Mode fracture conditions is adopted, to couple the modes of fracture:

$$\left(\frac{\mathcal{G}_I^i}{\mathcal{G}_{IC}^i}\right)^2 + \left(\frac{\mathcal{G}_{II}^i}{\mathcal{G}_{IIC}^i}\right)^2 + \left(\frac{\mathcal{G}_{III}^i}{\mathcal{G}_{IIIC}^i}\right)^2 = 1. \tag{42}$$

Finally, the following tangent constitutive operators at the interface are required for the subsequent

9

numerical treatment via nonlinear FEM:

$$\frac{\partial^2 \mathcal{G}_c^i}{\partial \mathbf{g}_{\text{loc}}^2} = \begin{bmatrix} \hat{\alpha} k_n & 0 & 0 \\ 0 & \hat{\beta} k_{t1} & 0 \\ 0 & 0 & \hat{\gamma} k_{t2} \end{bmatrix}, \tag{43a}$$

$$\frac{\partial^2 \mathcal{G}_c^i}{\partial \mathbf{g}_{\text{loc}} \partial \hat{\mathfrak{d}}_i} = \begin{bmatrix} g_n k_n \dfrac{\partial \hat{\alpha}}{\partial \hat{\mathfrak{d}}_i} & g_{t1} k_{t1} \dfrac{\partial \hat{\beta}}{\partial \hat{\mathfrak{d}}_i} & g_{t2} k_{t2} \dfrac{\partial \hat{\gamma}}{\partial \hat{\mathfrak{d}}_i} \end{bmatrix}, \tag{43b}$$

$$\frac{\partial^2 \mathcal{G}_c^i}{\partial \hat{\mathfrak{d}}_i \partial \mathbf{g}_{\text{loc}}} = \begin{bmatrix} g_n k_n \dfrac{\partial \hat{\alpha}}{\partial \hat{\mathfrak{d}}_i} \\ g_{t1} k_{t1} \dfrac{\partial \hat{\beta}}{\partial \hat{\mathfrak{d}}_i} \\ g_{t2} k_{t2} \dfrac{\partial \hat{\gamma}}{\partial \hat{\mathfrak{d}}_i} \end{bmatrix}, \tag{43c}$$

$$\frac{\partial^2 \mathcal{G}_c^i}{\partial \delta \hat{\mathfrak{d}}_i^2} = \frac{1}{2} g_n^2 k_n \frac{\partial^2 \hat{\alpha}}{\partial \hat{\mathfrak{d}}_i^2} + \frac{1}{2} g_{t1}^2 k_{t1} \frac{\partial^2 \hat{\beta}}{\partial \hat{\mathfrak{d}}_i^2} + \frac{1}{2} g_{t2}^2 k_{t2} \frac{\partial^2 \hat{\gamma}}{\partial \hat{\mathfrak{d}}_i^2}. \tag{43d}$$

In the previous derivations, the terms $\hat{\alpha}$, $\hat{\beta}$ and $\hat{\gamma}$ are given by

$$\hat{\alpha} = \frac{g_{nc,0}^2}{\left[(1 - \mathfrak{d}_i) g_{nc,0} + \mathfrak{d}_i g_{nc,1} \right]^2}, \tag{44a}$$

$$\hat{\beta} = \frac{g_{t1c,0}^2}{\left[(1 - \mathfrak{d}_i) g_{t1c,0} + \mathfrak{d}_i g_{t1c,1} \right]^2} \tag{44b}$$

$$\hat{\gamma} = \frac{g_{t2c,0}^2}{\left[(1 - \mathfrak{d}_i) g_{t2c,0} + \mathfrak{d}_i g_{t2c,1} \right]^2} \tag{44c}$$

Finally, note that due to the lack of reliable experimental data, the previous formulation can be simplified by assuming the same interface response for fracture Modes II and III.

4. Finite element formulation

This section briefly presents the finite element formulation corresponding to the bulk (Section 4.1) and the interface (Section 4.2). The discretization is presented for the kinematic and for the crack phase field variable. With respect to time discretization, we consider a finite time increment $\Delta \tau = t_{n+1}^{(k)} - t_n$, where t_n and $t_{n+1}^{(k)}$ are the previous converged state and the prospective current time step at the global iteration k, respectively. At time t_n the independent variables, namely the displacements, the incompatible modes and the crack fields are known. Therefore, the goal of the computation is the determination of these variables at time $t_{n+1}^{(k)}$. It is worth mentioning that the update of the incompatible strains requires a careful attention as is thoroughly described in [34].

4.1. Finite element model of the bulk: interpolation of the displacement field and the incompatible strains

For the boundary value problem for the bulk, standard discretization of the domain $\mathcal{B}_0$ is considered to be constructed via n_e non-overlapping elements, such that $\mathcal{B}_0 \approx \bigcup_{e=1}^{n_e} \mathcal{B}_0^{(e)}$. The discretization of the bulk is performed according to the solid shell concept [58, 59], being the parametric space identified as follows: $\mathcal{A} := \{ \boldsymbol{\xi} = (\xi^1, \xi^2, \xi^3) \in \mathbb{R}^3 \mid -1 \leq \xi^i \leq +1; i = 1, 2, 3 \}$, where (ξ^1, ξ^2) denote in-plane directions, whereas ξ^3 identifies the thickness direction and H is the initial shell thickness.

The reference position vector of any material point (Fig. 3) is linearly interpolated by the position of the top $\mathbf{X}_t(\xi^1, \xi^2)$ and bottom $\mathbf{X}_b(\xi^1, \xi^2)$ vectors:

$$\mathbf{X}(\boldsymbol{\xi}) = \frac{1}{2} \left(1 + \xi^3 \right) \mathbf{X}_t(\xi^1, \xi^2) + \frac{1}{2} \left(1 - \xi^3 \right) \mathbf{X}_b(\xi^1, \xi^2). \tag{45}$$

10

Similarly, the same interpolation scheme is adopted for the current configuration:

$$\mathbf{x}(\boldsymbol{\xi}) = \frac{1}{2}\left(1 + \xi^3\right)\mathbf{x}_t(\xi^1, \xi^2) + \frac{1}{2}\left(1 - \xi^3\right)\mathbf{x}_b(\xi^1, \xi^2). \tag{46}$$

The previous approximation is also assumed for the crack phase field

$$\mathfrak{d}(\boldsymbol{\xi}) = \frac{1}{2}\left(1 + \xi^3\right)\mathfrak{d}_t(\xi^1, \xi^2) + \frac{1}{2}\left(1 - \xi^3\right)\mathfrak{d}_b(\xi^1, \xi^2), \tag{47}$$

where $\mathfrak{d}_t$ and bottom $\mathfrak{d}_b$ stand for the crack phase field values corresponding to the top and bottom surfaces of the body, respectively. This ansazt for the phase field variable allows a non-uniform value of this parameter over the shell thickness, as discussed in [34].

Standard trilinear shape functions are used to interpolate the reference and current position vectors:

$$\mathbf{X} = \mathbf{N}(\boldsymbol{\xi})\widetilde{\mathbf{X}} \quad \text{and} \quad \mathbf{x} = \mathbf{N}(\boldsymbol{\xi})\widetilde{\mathbf{x}}, \tag{48}$$

where $\mathbf{N}(\boldsymbol{\xi})$ is the matrix operator associated with the shape functions.

Accordingly, the displacement and the phase field variable $(\mathbf{u}, \mathfrak{d})$, their respective variations $(\delta\mathbf{u}, \delta\mathfrak{d})$ and their increments $(\Delta\mathbf{u}, \Delta\mathfrak{d})$ are approximated at the element level as

$$\mathbf{u} \approx \mathbf{N}(\boldsymbol{\xi})\mathbf{d}; \ \delta\mathbf{u} \approx \mathbf{N}(\boldsymbol{\xi})\delta\mathbf{d}; \ \Delta\mathbf{u} \approx \mathbf{N}(\boldsymbol{\xi})\Delta\mathbf{d}, \tag{49}$$

$$\mathfrak{d} = \mathbf{N}(\boldsymbol{\xi})\overline{\mathfrak{d}}; \ \delta\mathfrak{d} = \mathbf{N}(\boldsymbol{\xi})\delta\overline{\mathfrak{d}}; \ \Delta\mathfrak{d} = \mathbf{N}(\boldsymbol{\xi})\Delta\overline{\mathfrak{d}}. \tag{50}$$

The interpolation of the incompatible strain field is expressed in terms of the operator $\mathbf{M}(\boldsymbol{\xi})$ that is designed to alleviate membrane and Poisson thickness locking pathologies can be performed by the used of the EAS method. The interpolation of the incompatible strains $\tilde{\mathbf{E}}$, its variation $\delta\tilde{\mathbf{E}}$ and its increment $\Delta\tilde{\mathbf{E}}$ renders

$$\tilde{\mathbf{E}} \approx \mathbf{M}(\boldsymbol{\xi})\boldsymbol{\varsigma}, \ \delta\tilde{\mathbf{E}} \approx \mathbf{M}(\boldsymbol{\xi})\delta\boldsymbol{\varsigma}, \ \Delta\tilde{\mathbf{E}} \approx \mathbf{M}(\boldsymbol{\xi})\Delta\boldsymbol{\varsigma}, \tag{51}$$

The particular form of the interpolation operator in the local parametric setting $(\tilde{\mathbf{M}}(\boldsymbol{\xi}))$ is given by [60]

$$\tilde{\mathbf{M}}(\boldsymbol{\xi}) = \begin{bmatrix} \xi^1 & 0 & 0 & 0 & 0 & 0 & 0 \\ 0 & \xi^2 & 0 & 0 & 0 & 0 & 0 \\ 0 & 0 & \xi^3 & \xi^1\xi^3 & \xi^2\xi^3 & 0 & 0 \\ 0 & 0 & 0 & 0 & 0 & \xi^1 & \xi^2 \\ 0 & 0 & 0 & 0 & 0 & 0 & 0 \\ 0 & 0 & 0 & 0 & 0 & 0 & 0 \end{bmatrix}. \tag{52}$$

As discussed in [45, 61], the operator $\tilde{\mathbf{M}}(\boldsymbol{\xi})$ is subsequently transformed into the global Cartesian setting in order to preserve the consistency of the formulation. Furthermore, in the current solid shell model, transverse shear and trapezoidal locking are circumvented through the use of the assumed natural strain method as detailed in [34].

Insertion of the previous discretization schemes into the residual forms given in Eqs.(17)–(19), and into the corresponding linearized system, Eqs.(20)–(22), leads to the following coupled system

$$\begin{bmatrix} \mathbf{k}_{dd} & \mathbf{k}_{d\mathfrak{d}} & \mathbf{k}_{d\varsigma} \\ \mathbf{k}_{\mathfrak{d}d} & \mathbf{k}_{\mathfrak{d}\mathfrak{d}} & \mathbf{k}_{\mathfrak{d}\varsigma} \\ \mathbf{k}_{\varsigma d} & \mathbf{k}_{\varsigma\mathfrak{d}} & \mathbf{k}_{\varsigma\varsigma} \end{bmatrix} \begin{bmatrix} \Delta\mathbf{d} \\ \Delta\overline{\mathfrak{d}} \\ \Delta\boldsymbol{\varsigma} \end{bmatrix} = \begin{bmatrix} \mathbf{R}^d_{\text{ext}} \\ \mathbf{0} \\ \mathbf{0} \end{bmatrix} - \begin{bmatrix} \mathbf{R}^d_{\text{int}} \\ \mathbf{R}^{\mathfrak{d}}_{\text{int}} \\ \mathbf{R}^{\varsigma}_{\text{int}} \end{bmatrix}. \tag{53}$$

This system can be reduced due to the static condensation of the incompatible strains at the element level [34], so that the final system reads of equations featuring the coupled scheme between the kinematic and the phase field yields

$$\begin{bmatrix} \mathbf{k}^*_{dd} & \mathbf{k}^*_{d\mathfrak{d}} \\ \mathbf{k}^*_{\mathfrak{d}d} & \mathbf{k}^*_{\mathfrak{d}\mathfrak{d}} \end{bmatrix} \begin{bmatrix} \Delta\mathbf{d} \\ \Delta\overline{\mathfrak{d}} \end{bmatrix} = \begin{bmatrix} \mathbf{R}^d_{\text{ext}} \\ \mathbf{0} \end{bmatrix} - \begin{bmatrix} \mathbf{R}^{d*}_{\text{int}} \\ \mathbf{R}^{\mathfrak{d}*}_{\text{int}} \end{bmatrix} \tag{54}$$

11

where the modified residuals and tangent matrices take the form

$$\mathbf{k}_{dd}^* = \mathbf{k}_{dd} - \mathbf{k}_{d\varsigma}\mathbf{k}_{\varsigma\varsigma}^{-1}\mathbf{k}_{\varsigma d}, \quad \mathbf{k}_{d\mathfrak{d}}^* = \mathbf{k}_{d\mathfrak{d}} - \mathbf{k}_{d\varsigma}\mathbf{k}_{\varsigma\varsigma}^{-1}\mathbf{k}_{\varsigma\mathfrak{d}}, \tag{55}$$

$$\mathbf{k}_{\mathfrak{d}d}^* = \mathbf{k}_{\mathfrak{d}d} - \mathbf{k}_{\mathfrak{d}\varsigma}\mathbf{k}_{\varsigma\varsigma}^{-1}\mathbf{k}_{\varsigma d}, \quad \mathbf{k}_{\mathfrak{d}\mathfrak{d}}^* = \mathbf{k}_{\mathfrak{d}\mathfrak{d}} - \mathbf{k}_{\mathfrak{d}\varsigma}\mathbf{k}_{\varsigma\varsigma}^{-1}\mathbf{k}_{\varsigma\mathfrak{d}}, \tag{56}$$

$$\mathbf{R}_{\text{int}}^{d*} = \mathbf{R}_{\text{int}}^{d} - \mathbf{k}_{d\varsigma}\mathbf{k}_{\varsigma\varsigma}^{-1}\mathbf{R}_{\text{int}}^{\varsigma}, \quad \mathbf{R}_{\text{int}}^{\mathfrak{d}*} = \mathbf{R}_{\text{int}}^{\mathfrak{d}} - \mathbf{k}_{\mathfrak{d}\varsigma}\mathbf{k}_{\varsigma\varsigma}^{-1}\mathbf{R}_{\text{int}}^{\varsigma}. \tag{57}$$

The algebraic system in Eq.(54) is solved using a monolithic Newton-Raphson procedure, which constitutes a robust scheme for the developed modeling framework.

4.2. Finite element model at the interface

In line with the previous derivations, we construct the finite element discretization of the proposed 3D geometrical nonlinear interface model compatible with the phase field approach of fracture in the bulk. As customary, this requires the definition of a reference surface (usually the interface midsurface). The parametric space is defined as $\bar{\boldsymbol{\xi}} = \{\xi^1, \xi^2\} \in [\text{-}1,1]\times[\text{-}1,1]$, where ξ^1, ξ^2 denote the natural coordinates of the interface, and $\mathbf{N}(\bar{\boldsymbol{\xi}})$ identifies the operator arranging the interface shape functions in matrix notation.

Applying standard arguments, the interpolation of the local gap vector can renders

$$\mathbf{g}_{\text{loc}} = \mathbf{R}(\mathbf{d}_i)\hat{\mathbf{B}}_{\mathbf{b}}\mathbf{d}_i, \tag{58}$$

where $\hat{\mathbf{B}}_{\mathbf{b}} = \mathbf{L}\mathbf{N}$ is the interface compatibility operator, and $\mathbf{d}_i$ denotes the vector collecting the nodal displacements of the interface flanks. Therefore, the discrete variation and increment of the local gap vector are given by

$$\delta\mathbf{g}_{\text{loc}} = \left[\frac{\partial\mathbf{R}(\mathbf{d}_i)}{\partial\mathbf{d}_i}\hat{\mathbf{B}}_{\mathbf{b}}\mathbf{d}_i + \mathbf{R}(\mathbf{d}_i)\hat{\mathbf{B}}_{\mathbf{b}}\right]\delta\mathbf{d}_i; \quad \Delta\mathbf{g}_{\text{loc}} = \left[\frac{\partial\mathbf{R}(\mathbf{d}_i)}{\partial\mathbf{d}_i}\hat{\mathbf{B}}_{\mathbf{b}}\mathbf{d}_i + \mathbf{R}(\mathbf{d}_i)\hat{\mathbf{B}}_{\mathbf{b}}\right]\Delta\mathbf{d}_i, \tag{59}$$

whilst the discrete linearized virtual local gap reads

$$\Delta\delta\mathbf{g}_{\text{loc}} \approx \left[2\frac{\partial\mathbf{R}(\mathbf{d}_i)}{\partial\mathbf{d}_i}\hat{\mathbf{B}}_{\mathbf{b}}\delta\mathbf{d}_i\right]\Delta\mathbf{d}_i \tag{60}$$

In an analogous manner, the crack phase field variable, its variation and its increment are interpolated as the interface as follows

$$\mathfrak{d}_i = \hat{\mathbf{B}}_{\mathfrak{d}}\bar{\mathfrak{d}}_i, \quad \delta\mathfrak{d}_i = \hat{\mathbf{B}}_{\mathfrak{d}}\delta\bar{\mathfrak{d}}_i, \quad \Delta\mathfrak{d}_i = \hat{\mathbf{B}}_{\mathfrak{d}}\Delta\bar{\mathfrak{d}}_i \tag{61}$$

where $\hat{\mathbf{B}}_{\mathfrak{d}}$ is the compatibility operator corresponding to the crack phase field variable, and $\bar{\mathfrak{d}}_i$ stands for the nodal phase field values at the interface flanks.

Finally, through the insertion the approximations given above into the residual, Eqs.(30)-(31), and linearized forms, Eqs.(32)-(33), the following coupled algebraic systems can be obtained:

$$\begin{bmatrix} \mathbf{k}_{\mathbf{d}\mathbf{d}}^i & \mathbf{k}_{\mathbf{d}\mathfrak{d}}^i \\ \mathbf{k}_{\mathfrak{d}\mathbf{d}}^i & \mathbf{k}_{\mathfrak{d}\mathfrak{d}}^i \end{bmatrix} \begin{bmatrix} \Delta\mathbf{d}_i \\ \Delta\bar{\mathfrak{d}}_i \end{bmatrix} = \begin{bmatrix} \mathbf{f}_d^i \\ \mathbf{f}_{\mathfrak{d}}^i \end{bmatrix}. \tag{62}$$

Note that in line with the bulk formulation, the system given in Eq.(62) is solved via a monolithic Newton-Raphson method.

5. Numerical examples

In this section, the modelling capabilities of the proposed 3D computational framework coupling the PF approach of fracture and the CZM for interface cracking for finite elasticity are assessed through several examples. The main objective of these simulations concerns showing the ability of the proposed model to simulate different crack propagation paths in heterogeneous materials and engineering structural components with different geometries. In many practical applications, heterogeneous materials and composite structures

posses several interfaces, which provoke the development of complex crack patterns due to the interaction between the crack propagation in the bulk and delamination events at the existing interfaces.

In the first example we aim at showing the effect of the interaction between the PF and the CZM within the proposed model. A tensile test of a flat single-edge notched specimen of a homogeneous material is then considered. The second and third examples illustrate the potentialities of the combined use of the enhanced-based solid shell formulation together with the 3D interface. These applications comprise the simulation of heterogeneous specimens using out-of-plane loading with planar structures (second example), and membrane loading with curved geometry (third example). Finally, an experimental case study regarding fracture predictions in photovoltaic (PV) panels is considered. In particular, a 4-point bending test of a solar panel is simulated, being the corresponding results correlated with experimental data taken from the related literature. All the simulations have been performed with the finite element program FEAP [62]. Dirichlet boundary conditions applied with a monotonically increasing law are defined in the numerical examples herein addressed.

5.1. Single-edge notched specimen

The first insight onto the potentialities of the proposed model is presented by means of the simulation of a flat single-edge notched specimen under uniform tensile loading. The geometry of the specimen is shown in Fig. 4. An interface perpendicular to a middle notch runs along all the length of the specimen. A prescribed displacement along the y-direction is prescribed at the top and bottom edges of the specimen, see Fig. 4. The material parameter used are collected in Table 1.

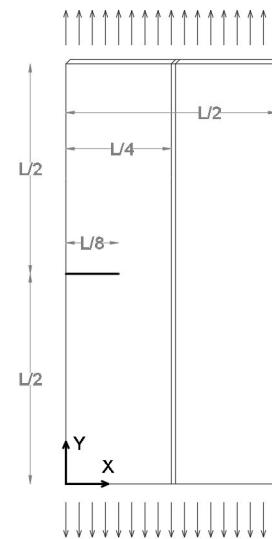| Geometry parameters		
L	1 mm	Plate length
t	0.003 mm	Plate thickness
h	0.0001 mm	Interface thickness
Mechanical parameters for the PF model		
E_b	3240 MPa	Bulk Young modulus
v_b	0.35	Bulk Poisson ratio
G_b	0.35 N/mm	Bulk fracture energy
l_b	0.02 mm	Phase Filed length scale parameter
G_i	0.35 N/mm	Interface fracture energy for mode I, mode II and mode III
σ_{max}	$1000 \div 75$ MPa	Interface maximum tensile traction for mode I, mode II and mode III
$g_{c,0}$	$7e\text{-}4 \div 0.014$ mm	Interface initial critical opening for mode I, mode II and mode III
$g_c/g_{c,0}$	$1 \div 5$	Interface opening ratio for mode I, mode II and mode III

Table 1: Geometry and material parameters.

Figure 4: Specimen geometry.

Several simulations with various interface parameters have been performed in order to show the different crack patterns that can be activated. According to [63], the occurrence of delamination together with crack propagation is governed by the interface maximum tensile traction. These authors claimed that when the length of the initial delamination or crack penetration is much smaller then the global dimension, crack deflection is confined within the stress field. In line with these considerations, in the system defined in Fig. 4, the global dimension L is much larger than the crack penetration/delamination length (the specific ratio between those dimensions is higher than 10). Therefore, we focus our parametric analysis on the variation of the peak traction of the interface in order to evaluate the accuracy of the proposed method with respect to linear elastic fracture mechanics predictions.

The computational model herein used is composed of 11794 nodes. The mesh is refined in correspondence of the centre of the specimen to achieve the convergence during crack propagation. The maximum tensile

(Mode I) traction of the CZM has been increased from 75 MPa to 1000 MPa. Moreover, the final interface critical opening for $\mathfrak{d} = 1$ (g_c) takes the following values: $g_c = g_{c,0}$, $2g_{c,0}$, $5g_{c,0}$. The general evolution of the simulations is shown in Fig. 5 for each of the cases defined above. In this graph it can be observed that the crack propagates straight in the bulk, and when imping on the interface two scenarios might occur depending on the interface peak traction: (1) no delamination is developed at the interface and the crack starts propagating in the right bulk; (2) delamination occurs at the interface, so that the crack propagation in the adjacent bulk is delayed.

This behaviour can be recognized from the force-displacement curves in Fig. 6. In particular, when delamination occurs, the curve is characterized by two drops in carrying capacity of the system: the first kink corresponds to the failure of the left part and the second one is associated with the failure of the right part. This concurrence of crack propagation and delamination is obtained for 75 MPa $< \sigma_{\max} <$ 250 MPa. For values of $\sigma_{\max} \geq$ 250 MPa, the interface is stiff enough such that the crack propagates in the bulk without delamination.

(a) Crack impinging on the interface

(b) Specimen failure

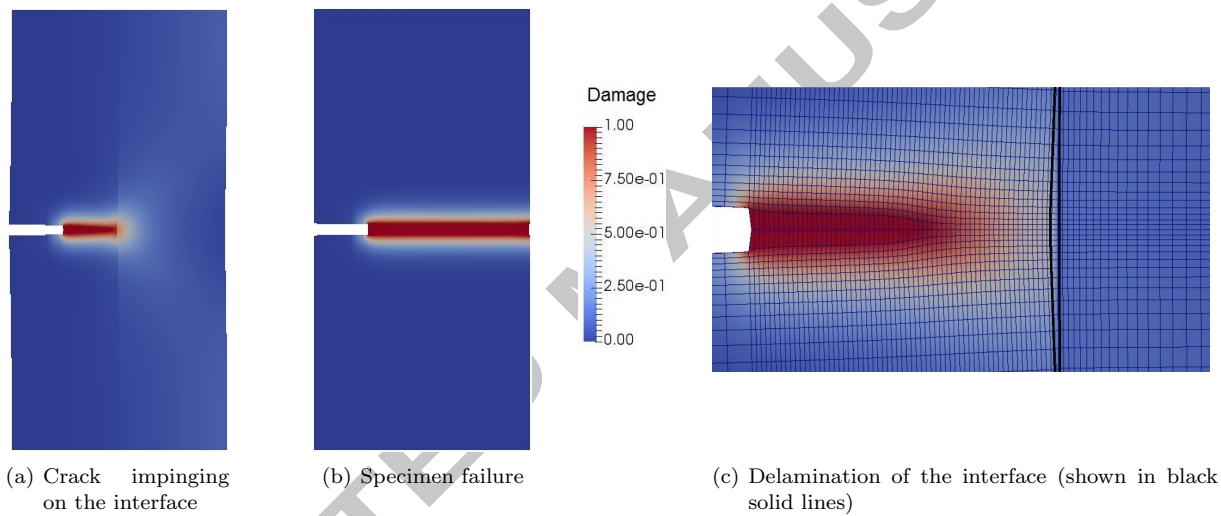(c) Delamination of the interface (shown in black solid lines)

Figure 5: (a) & (b) two steps of crack propagation; (c) close-up view of delamination when the crack is approaching the interface.

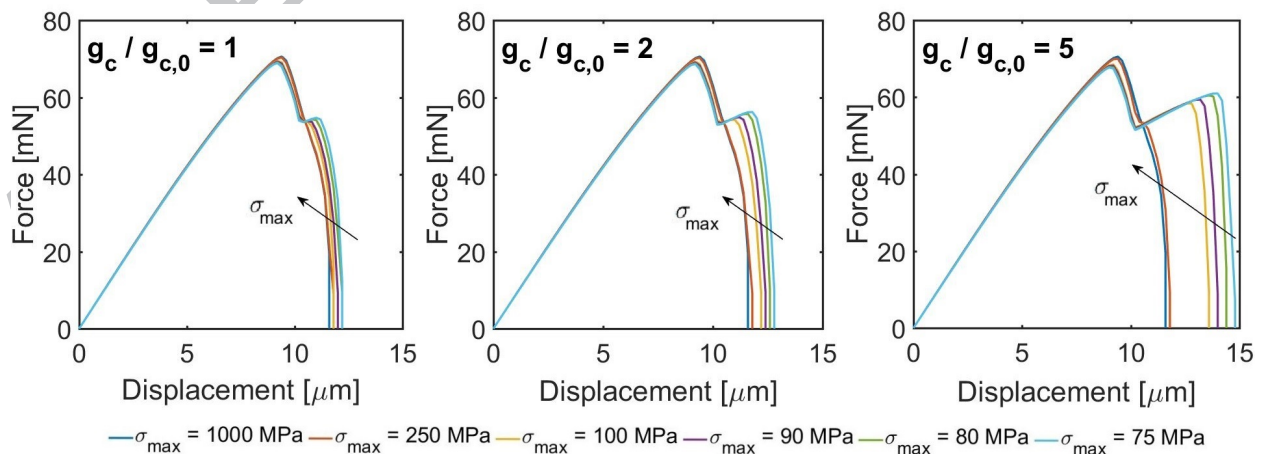Figure 6: Force displacement curve varying $\sigma_{\max}$ and the ratio $g_c/g_{c,0}$. The arrow shows the direction of increasing of $\sigma_{\max}$

14

The ratio $g_c/g_{c,0}$, which governs the coupling between the PF and the CZM, is also affecting the fracture predictions. High values of this ratio cause longer delamination paths. In fact, when $g_c/g_{c,0} > 1$, the damage in the bulk makes the interface more compliant and consequently the actual σ_{max} decreases according to the present model. Under this condition, delamination is triggered earlier. As a side effect, the crack propagation into the adjacent layer is delayed. This behaviour can be identified also in the force-displacement curve in Fig. 6 through observing that the second drop in the evolution curve is predicted to take place for larger displacements as $g_c/g_{c,0}$ increases.

5.2. Flat sandwich panel under 4-point bending and tension

This example concerns the fracture of a flat sandwich panel subjected to combined in-plane and out-of-plane loading (Fig. 7). The sandwich panel is made of three brittle layers with an interface between each layer. The topmost layer is characterized by a notch in the middle of the span that runs along over the complete width of the specimen, whereas its depth is equal to half its thickness. The topmost and the bottommost layers are assumed to have the same material parameters, while the middle layer is made of a stiffer material (Fig. 8). All the relevant material parameters used in the present application are reported in Table 2.
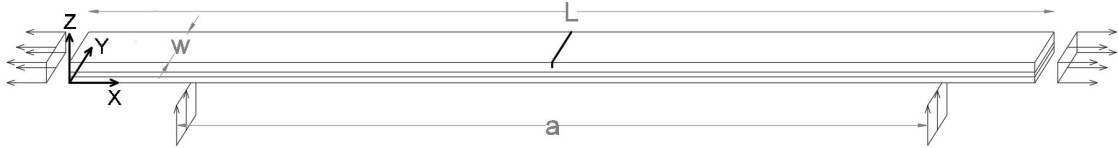

Figure 7: Geometry of the 4-point-bending specimen.

Geometry parameters		
L	2 mm	Panel length
w	0.5 mm	Panel width
a	1.556 mm	Bending span
t	0.01 mm	Main thickness
h	0.001 mm	Interface thickness
Mechanical parameters		
E_1	100 GPa	Material 1 Young modulus
v_1	0.3	Material 1 Poisson ratio
G_1	0.5 N/mm	Material 1 fracture energy
l_1	0.05 mm	Material 1 Phase Filed parameter
E_2	200 GPa	Material 2 Young modulus
v_2	0.2	Material 2 Poisson ratio
G_2	1.0 N/mm	Material 2 fracture energy
l_2	0.05 mm	Material 2 Phase Filed parameter
G_i	0.5 N/mm	Interface fracture energy for Mode I, Mode II and Mode III
σ_{max}	$1000 \div 0.01$ GPa	Interface maximum tensile stress for Mode I, Mode II and Mode III
$g_c/g_{c,0}$	1	Interface opening ratio for Mode I, Mode II and Mode III

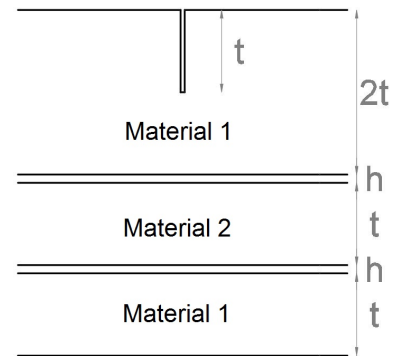Table 2: Sandwich panel geometry and material parameters.

Figure 8: Sandwich panel structure along the thickness.

By exploiting the symmetry of the system and of the applied boundary conditions, we consider only half domain for the simulations. The model has 12376 nodes and is refined in proximity of the notch. Two different simulations are carried out: the first simulation concerns with a strong interface ($\sigma_{max} = 1 \times 10^6$ MPa), where the second case comprises a weak interface definition ($\sigma_{max} = 10$ MPa).

In the simulation with a stronger interface, damage evolution is predicted to at the notch (Fig. 9(a)), and the final failure follows immediately after crack propagation (Fig. 9(b)). Numerical results predict bulk failure without any delamination. On the contrary, for a weaker interface ($\sigma_{max} = 10$ MPa), the failure

15

sequence follows this order: (1) an initial failure of the topmost notched layer (Figs. 10(a),), (2) propagation interfacial delamination between the topmost and the middle layer (Figs. 10(b)), (3) bulk failure of the middle layer (Figs. 10(c)), (4) delamination between the middle and the bottommost layer (Figs. 10(d)), (5) failure of the bottommost layer (Figs. 10(e)).

Fig. 11 depicts the reaction force vs. the out-of-plane displacement curves for the above two scenarios. The strong interface evolution shows an initial nearly linear behaviour. Subsequently, nonlinear effects attributed to the deformation process and bulk damage can be identified. Finally, the absence of interface delamination leads to a characteristics brittle failure of the specimen upon failure. Conversely, the case including a weaker interface exhibits a much different response. Analysing the red curve in Fig. 11, it can be observed that nonlinear effects occur for much lower displacements due to the combination three aspects: (1) the presence of geometrically bending deformation effects, (2) the development of bulk damage in the topmost layer, and (3) the onset and growth of delamination events which are provoked for the different stiffness values between adjacent layers. Moreover, at advanced stages, the evolution is characterized by several load drops. Specifically, these drops are directly associated with the failure of each of the composing layers, which concomitantly evolves with the progression of delamination along the adjoining interfaces.

(a) Damage in the topmost layer (b) Damage at specimen failure
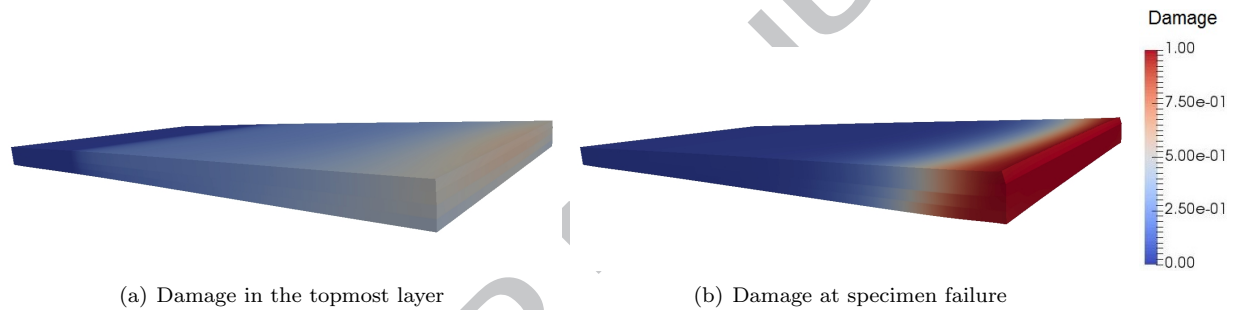
Figure 9: Damage contour plot of the flat sandwich panel under tension and 4-point bending for the case of strong interfaces, showing crack through the specimen without delamination

5.3. Cylinder under tension

The proposed methodology is further examined in relation to a cylindrical geometry whose dimensions are: length $L = 2$ mm, external diameter $d_{\text{ext}} = 0.72$ mm, and inner diameter $d_{\text{int}} = 0.678$ mm (Fig. 12). The same material parameters used in Section 5.2 are considered, including the strong and weak interface cases. The external layer is characterized by a notch which runs around all the circumference and its depth is half of its thickness. Due to the symmetry of the problem, the simulations are performed by considering 1/8 of the total domain. The FE discretization presents by 13824 nodes. The specimen is loaded under tensile displacement along the x-direction.

Fig. 13 shows the force-displacement curves for a strong interface ($\sigma_{\text{max}} = 1\text{x}10^6$ MPa) and a weak interface ($\sigma_{max} = 10$ MPa). For the current application, delamination at each interface are predicted to take place for very small imposed displacements, simultaneously with bulk crack propagation. This response stems from the fact that there are no bending effects. Therefore, the nonlinear evolution of both curves before the first drop in the load-carrying capacity is mostly due to the development of damage in the external layer. Furthermore, for the strong interface case, the failure is characterized by an almost perfect brittle evolution (sudden drop). In contrast, the weak interface scenario features a post-peak response as that noted in Section 5.2, from a qualitative standpoint (Fig. 14).
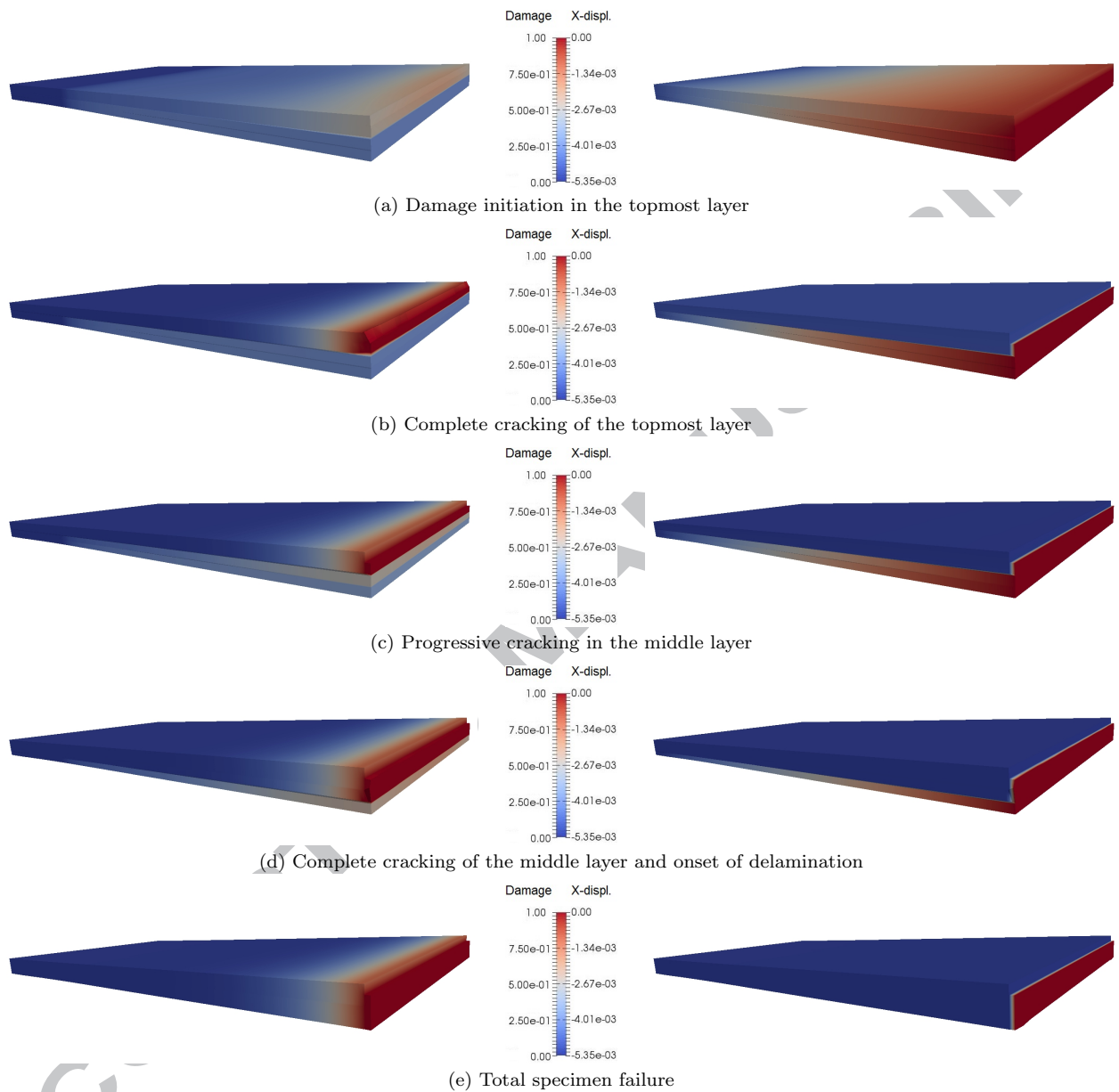
16

(a) Damage initiation in the topmost layer

(b) Complete cracking of the topmost layer

(c) Progressive cracking in the middle layer

(d) Complete cracking of the middle layer and onset of delamination

(e) Total specimen failure

Figure 10: Crack propagation and delamination evolution of the flat sandwich panel under tension and 4-point bending, for weak interface layer

5.4. Crack propagation in a solar photovoltaic panel

The last numerical example concerns the simulation of a 4-point bending experimental test of a photovoltaic (PV) module. The experimental test was performed and comprehensively described in [64]. A typical PV module is composed of 5 different layers (Fig. 15(a)): the middle layer is made of solar cells, which are encapsulate in an adhesive material made of EVA, while the topmost and bottommost layers are made of glass and PET, respectively.

The experimental set-up and the specimen geometry are shown in (Fig. 15(b)). The panel is composed of 10 solar cells, which were disposed along two parallel rows (5 cells per row). An electroluminescence camera was positioned on top of the middle line in order to detect microcrack patterns. The experimental tests
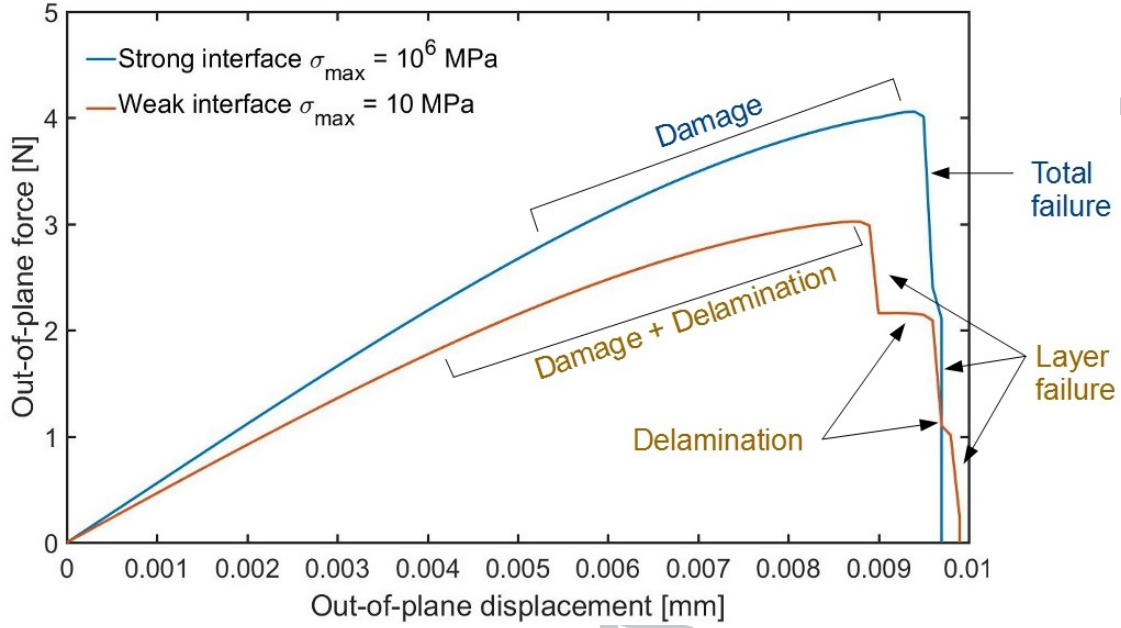
17

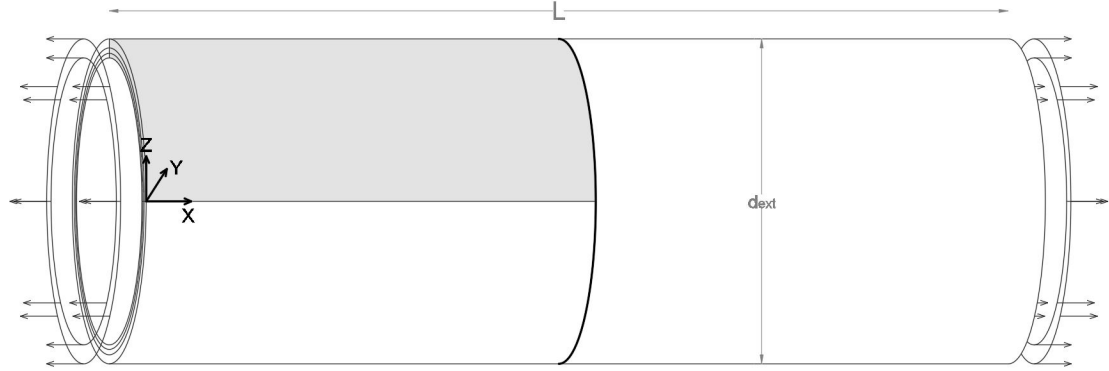Figure 11: Force-displacement curve of the sandwich panel under tension and 4-point-bending

Figure 12: Geometry of the cylinder tension test. In grey is highlighted the symmetric domain considered for the simulation.

were conducted on specimens with busbars parallel or perpendicular to the applied displacement direction. Recalling the analysis carried out in [64], in the current investigation, we only consider the PV panel configuration with parallel busbars, where crack events are mostly concentrated along the middle line of the specimen.

The numerical model herein used to reproduce the experimental results comprises 11172 nodes. Again, the exploitation of symmetry conditions allows the discretization of just one quarter of the panel. The relevant material parameters for this test are collected in Table 3 complying within standard PV panels [65]. The middle layer of the specimen, corresponding to the solar cells, is modelled as a homogeneous single layer 0.166 mm thick with material properties of brittle Silicon (Si) (Table 3). The regularization parameter l_{Si} of the PF model for the Si layer is set equal to 0.04 mm.

The EVA layers are 0.5 mm thick and the corresponding material properties, which strongly depend on temperature, are evaluated at room temperature. The bottommost PET layer and the topmost glass layer have a thickness equal to 0.1 mm and 2.55 mm, respectively. In between the Si and the EVA layers, interfaces 0.001 mm thick are introduced. Only phase field fracture is the Silicon layer is allowed, due to its
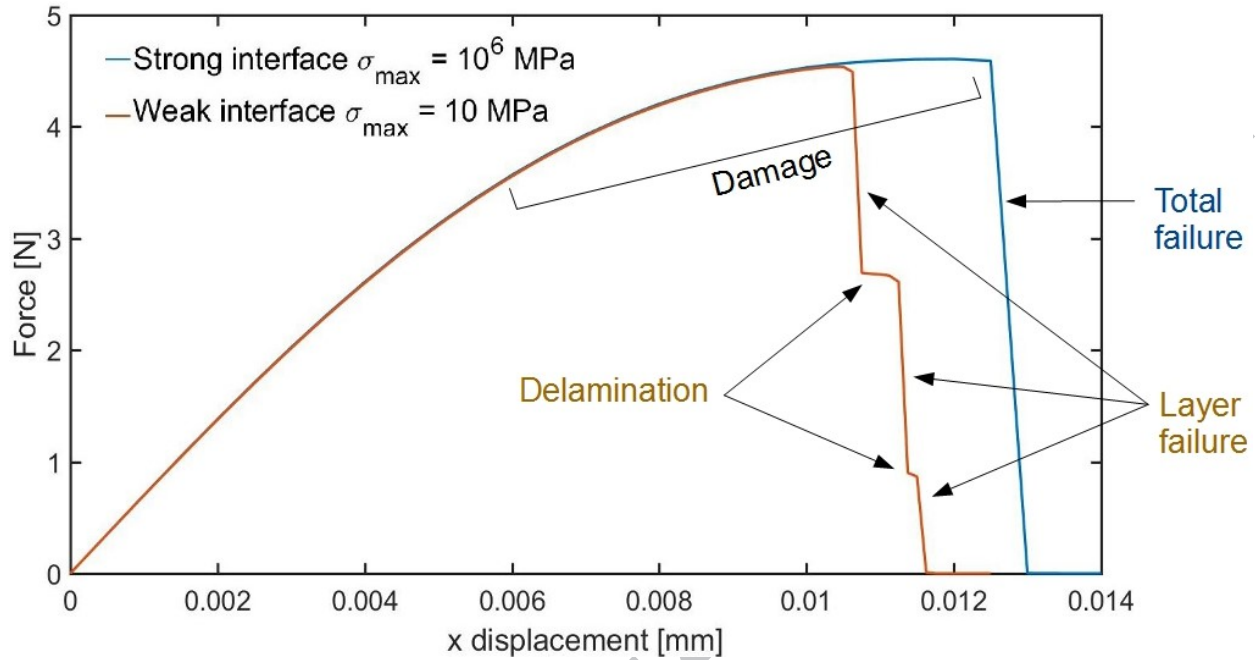
18

Figure 13: Force-displacement curves of the cylinder under tension

brittleness, and its competition with interface delamination is investigated.

The load-displacement curves corresponding to the experimental data and to the numerical predictions are shown in Fig. 16. The specimen response was characterized by an initial proportional load-displacement evolution up to a load level of around 800 N. This initial stage is satisfactorily reproduced by the current numerical method. Progressing along the loading application, the experimental evolution features a moderate variation of the stiffness of the specimen due to the development of microcracking phenomena in the Si cells. Analysing the corresponding numerical prediction, the present model enables capturing the load level at which this drop took place in the load-displacement curve with good accuracy. However, due to the fact that the present simulation devices a uniform Si layer instead of a cell-wise model, it is not possible to simulate the growth of multiple small cracks. This fact yields a load drop concentrated in one single event, rather than due to multiple cracks propagation. Nevertheless, it can be observed that at the final stage of such evolution an (when cracking affected all the solar cells throughout the middle line of the panel), the numerical model captures the final stiffness of the panel, consistently with the experimental results. The deformed configuration at failure is shown in Fig.17(a) and cracking in the Si layer is shown in Fig.17(b).

6. Conclusions

In the present study, a computational framework to simulate interlayer and intralayer crack propagation in composite structures has been proposed for three-dimensional large deformation problems. The Phase Field model for brittle fracture has been implemented within the solid shell formulation for thin walled structures. This model has been consistently coupled with a novel CZM for Mode I, II and III for the simulation of interlayer delamination, which has been coded within interface finite elements for large displacements. Coupling between the two models of fracture has been achieved by considering a reduction of the cohesive zone model stiffness with the increasing amount of damage $\mathfrak{d}$ at the surrounding bulk. In this way many complex crack paths in composite materials can be reproduced, precluding the use of any crack tracking or remeshing algorithm.

(a) Complete cracking of the topmost layer

(b)

(c) Progressive cracking in the middle layer

(d) Complete cracking of the middle layer and onset of delamination
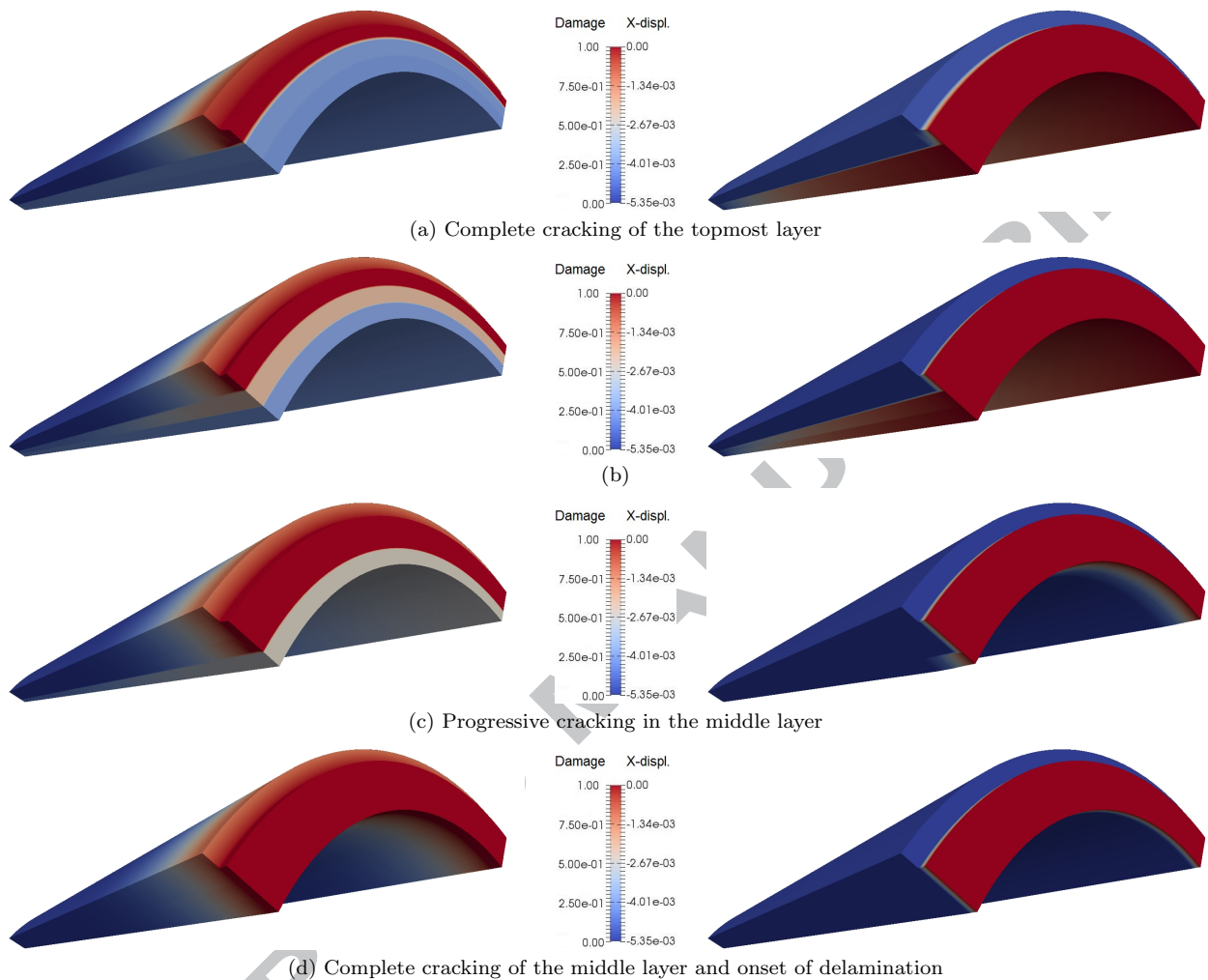
Figure 14: Crack propagation and delamination evolution of the sandwich panel with cylindrical geometry under tension, for weak interface layer

Several numerical examples, concerning the crack propagation in a flat geometry, in a flat and curved sandwich panel and in a PV solar panel, have been used to validate the proposed computational model, and have shown its ability to simulate complex crack phenomena. The interaction between intralayer crack propagation and interlayer delamination can be captured including patterns with concurrent delamination and crack propagation. Moreover, the potentialities of the solid shell formulation can be exploited by simulating curved geometries and/or out-of-plane loading.

The model herein presented fosters new possibilities for the three-dimensional simulation of failure in composite materials. In this concern, it has been shown that the proposed numerical framework opens new possibilities with regard to the accurate stress analysis in composite photovoltaic modules and the simulation of material-related failures related to brittle cracking in Silicon or backsheet delamination due to cohesion failure of the encapsulant material.

Acknowledgments

20

(a) PV panel structure.

(b) Experimental test setup (distances in mm).
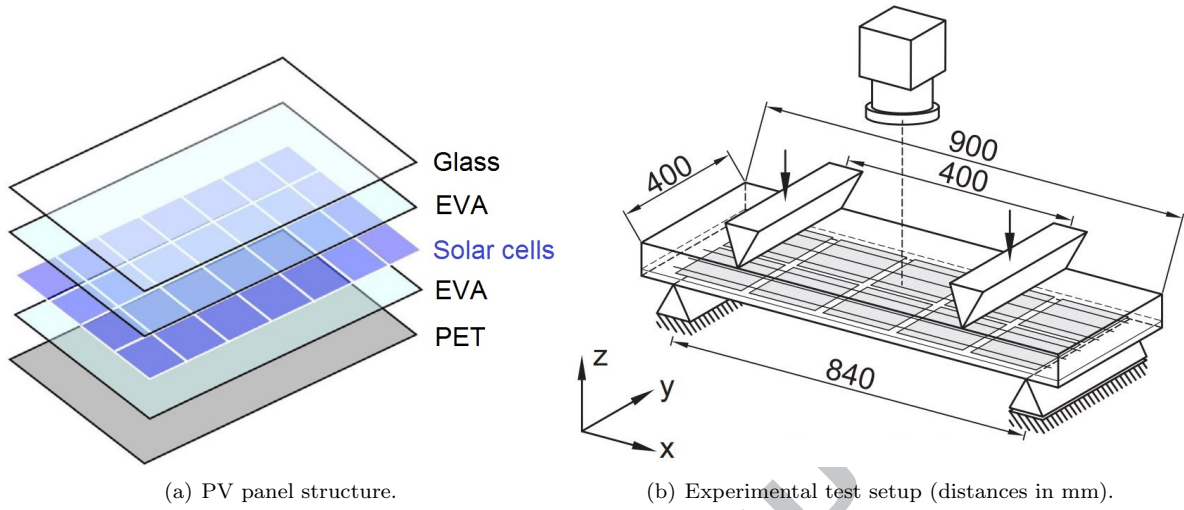
Figure 15: Geometry and boundary conditions of the specimen PV panel.

Mechanical parameters		
E_{Si}	130 GPa	Silicon Young modulus
v_{Si}	0.16	Silicon Poisson ratio
G_{Si}	0.0432 N/mm	Silicon fracture energy
l_{Si}	0.04 mm	Silicon Phase Filed parameter
E_{EVA}	0.004 GPa	EVA Young modulus
v_{EVA}	0.4	EVA Poisson ratio
E_{PET}	2.8 GPa	PET Young modulus
v_{PET}	0.37	PET Poisson ratio
E_{Gl}	73 GPa	Glass Young modulus
v_{Gl}	0.25	Glass Poisson ratio
G_i	100 N/mm	Interface fracture energy for Mode I, Mode II and Mode III
σ_{max}	1000 GPa	Interface maximum tensile stress for Mode I, Mode II and Mode III
$g_c/g_{c,0}$	1	Interface opening ratio for Mode I, Mode II and Mode III

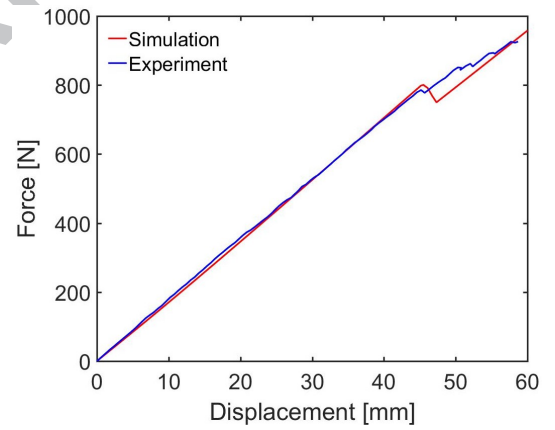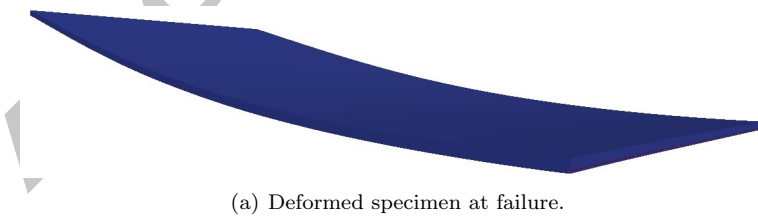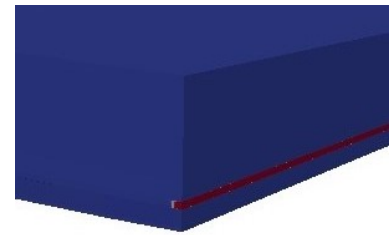Table 3: Sandwich panel geometry and material parameters.

Figure 16: Force displacement curve.

(a) Deformed specimen at failure.

(b) Zoom on the failure line.

Figure 17: Simulation.

21

References

[1] X-P Xu and A Needleman. Numerical simulations of fast crack growth in brittle solids. *Journal of the Mechanics and Physics of Solids*, 42(9):1397–1434, 1994.

[2] M Ortiz and A Pandolfi. Finite deformation irreversible cohesive elements for three-dimensional crack-propagation analysis. *International Journal for Numerical Methods in Engineering*, 44:1267–1282, 1999.

[3] N Moës, J Dolbow, and T Belytschko. A finite element method for crack growth without remeshing. *International journal for numerical methods in engineering*, 46(1):131–150, 1999.

[4] TP Fries and T Belytschko. The extended/generalized finite element method: an overview of the method and its applications. *International Journal for Numerical Methods in Engineering*, 84(3):253–304, 2010.

[5] JC Simo, J Oliver, and F Armero. An analysis of strong discontinuities induced by strain-softening in rate-independent inelastic solids. *Computational mechanics*, 12(5):277–296, 1993.

[6] J Oliver, AE Huespe, S Blanco, and DL Linero. Stability and robustness issues in numerical modeling of material failure with the strong discontinuity approach. *Computer Methods in Applied Mechanics and Engineering*, 195(52):7093–7114, 2006.

[7] C Linder and F Armero. Finite elements with embedded strong discontinuities for the modeling of failure in solids. *International Journal for Numerical Methods in Engineering*, 72(12):1391–1433, 2007.

[8] VA Lubarda, D Krajcinovic, and S Mastilovic. Damage model for brittle elastic solids with unequal tensile and compressive strengths. *Engineering Fracture Mechanics*, 49(5):681–697, 1994.

[9] M Jirásek. Nonlocal models for damage and fracture: comparison of approaches. *International Journal of Solids and Structures*, 35(31-32):4133–4145, 1998.

[10] M Frémond and B Nedjar. Damage, gradient of damage and principle of virtual power. *International Journal of Solids and Structures*, 33(8):1083 – 1103, 1996.

[11] RHJ Peerlings, MGD Geers, R De Borst, and WAM Brekelmans. A critical comparison of nonlocal and gradient-enhanced softening continua. *International Journal of solids and Structures*, 38(44):7723–7746, 2001.

[12] C Comi. Computational modelling of gradient-enhanced damage in quasi-brittle materials. *Mechanics of Cohesive-frictional Materials*, 4(1):17–36, 1999.

[13] C Comi and U Perego. Fracture energy based bi-dissipative damage model for concrete. *International journal of solids and structures*, 38(36):6427–6454, 2001.

[14] BJ Dimitrijevic and K Hackl. A regularization framework for damage–plasticity models via gradient enhancement of the free energy. *International Journal for Numerical Methods in Biomedical Engineering*, 27(8):1199–1210, 2011.

[15] N Moës, C Stolz, P-E Bernard, and N Chevaugeon. A level set based model for damage growth: the thick level set approach. *International Journal for Numerical Methods in Engineering*, 86(3):358–380, 2011.

[16] PE Bernard, N Moës, and N Chevaugeon. Damage growth modeling using the thick level set (tls) approach: Efficient discretization for quasi-static loadings. *Computer Methods in Applied Mechanics and Engineering*, 233:11–27, 2012.

[17] B Bourdin, GA Francfort, and J-J Marigo. The variational approach to fracture. *Journal of elasticity*, 91(1):5–148, 2008.

[18] L Ambrosio and VM Tortorelli. Approximation of functional depending on jumps by elliptic functional via t-convergence. *Communications on Pure and Applied Mathematics*, 43(8):999–1036, 1990.

[19] GA Francfort and J-J Marigo. Revisiting brittle fracture as an energy minimization problem. *Journal of the Mechanics and Physics of Solids*, 46(8):1319–1342, 1998.

[20] H Amor, J-J Marigo, and C Maurini. Regularized formulation of the variational brittle fracture with unilateral contact: numerical experiments. *Journal of the Mechanics and Physics of Solids*, 57(8):1209–1229, 2009.

[21] C Miehe, M Hofacker, and F Welschinger. A phase field model for rate-independent crack propagation: Robust algorithmic implementation based on operator splits. *Computer Methods in Applied Mechanics and Engineering*, 199(45):2765–2778, 2010.

[22] C Miehe, F Welschinger, and M Hofacker. Thermodynamically consistent phase-field models of fracture: Variational principles and multi-field fe implementations. *International Journal for Numerical Methods in Engineering*, 83(10):1273–1311, 2010.

[23] M Hofacker and C Miehe. A phase field model of dynamic fracture: Robust field updates for the analysis of complex crack patterns. *International Journal for Numerical Methods in Engineering*, 93(3):276–301, 2013.

[24] MJ Borden, CV Verhoosel, MA Scott, TJR Hughes, and CM Landis. A phase-field description of dynamic brittle fracture. *Computer Methods in Applied Mechanics and Engineering*, 217:77–95, 2012.

[25] M Ambati, T Gerasimov, and L De Lorenzis. Phase-field modeling of ductile fracture. *Computational Mechanics*, 55(5):1017–1040, 2015.

[26] F Amiri, D Millán, M Arroyo, M Silani, and T Rabczuk. Fourth order phase-field model for local max-ent approximants applied to crack propagation. *Computer Methods in Applied Mechanics and Engineering*, 312:254–275, 2016.

[27] C Miehe, LM Schänzel, and H Ulmer. Phase field modeling of fracture in multi-physics problems. part i. balance of crack surface and failure criteria for brittle crack propagation in thermo-elastic solids. *Computer Methods in Applied Mechanics and Engineering*, 294:449–485, 2015.

[28] C Miehe, M Hofacker, L-M Schaenzel, and F Aldakheel. Phase field modeling of fracture in multi-physics problems. part ii. coupled brittle-to-ductile failure criteria and crack propagation in thermo-elastic–plastic solids. *Computer Methods in Applied Mechanics and Engineering*, 294:486–522, 2015.

[29] X Zhang, A Krischok, and C Linder. A variational framework to model diffusion induced large plastic deformation and phase field fracture during initial two-phase lithiation of silicon electrodes. *Computer Methods in Applied Mechanics and Engineering*, 312:51–77, 2016.

[30] F Amiri, D Millán, Y Shen, T Rabczuk, and M Arroyo. Phase-field modeling of fracture in linear thin shells. *Theoretical and Applied Fracture Mechanics*, 69:102–109, 2014.

[31] P Areias, T Rabczuk, and MA Msekh. Phase-field analysis of finite-strain plates and shells including element subdivision. *Computer Methods in Applied Mechanics and Engineering*, 312:322–350, 2016.

[32] M Ambati and L De Lorenzis. Phase-field modeling of brittle and ductile fracture in shells with isogeometric nurbs-based solid-shell elements. *Computer Methods in Applied Mechanics and Engineering*, 312:351–373, 2016.

[33] J Kiendl, M Ambati, L De Lorenzis, H Gomez, and A Reali. Phase-field description of brittle fracture in plates and shells. *Computer Methods in Applied Mechanics and Engineering*, 312:374–394, 2016.

[34] J Reinoso, M Paggi, and C Linder. Phase field modeling of brittle fracture for enhanced assumed strain shells at large deformations: formulation and finite element implementation. *Computational Mechanics*, pages 1–21, 2017.

[35] T-T Nguyen, J Yvonnet, Q-Z Zhu, M Bornert, and C Chateau. A phase-field method for computational modeling of interfacial damage interacting with crack propagation in realistic microstructures obtained by microtomography. *Computer Methods in Applied Mechanics and Engineering*, 312:567–595, 2016.

[36] T-T Nguyen, J Yvonnet, M Bornert, and C Chateau. Initiation and propagation of complex 3d networks of cracks in heterogeneous quasi-brittle materials: direct comparison between in situ testing-microct experiments and phase field simulations. *Journal of the Mechanics and Physics of Solids*, 95:320–350, 2016.

[37] M Paggi and J Reinoso. Revisiting the problem of a crack impinging on an interface: a modeling framework for the interaction between the phase field approach for brittle fracture and the interface cohesive zone model. *Computer Methods in Applied Mechanics and Engineering*, 2017.

[38] M Aßmus, K Naumenko, and H Altenbach. A multiscale projection approach for the coupled global–local structural analysis of photovoltaic modules. *Composite Structures*, 158:340–358, 2016.

[39] Alfonso Pagani and Erasmo Carrera. Large-deflection and post-buckling analyses of laminated composite beams by carrera unified formulation. *Composite Structures*, 170:40–52, 2017.

[40] Enrico Zappino, Guohong Li, Alfonso Pagani, and Erasmo Carrera. Global-local analysis of laminated plates by node-dependent kinematic finite elements with variable esl/lw capabilities. *Composite Structures*, 172:1–14, 2017.

[41] Marco Paggi, Irene Berardone, Andrea Infuso, and Mauro Corrado. Fatigue degradation and electric recovery in silicon solar cells embedded in photovoltaic modules. *Scientific reports*, 4, 2014.

[42] Marco Paggi, Mauro Corrado, and Irene Berardone. A global/local approach for the prediction of the electric response of cracked solar cells in photovoltaic modules under the action of mechanical loads. *Engineering Fracture Mechanics*, 168:40–57, 2016.

[43] Marco Paggi, Mauro Corrado, and Maria Alejandra Rodriguez. A multi-physics and multi-scale numerical approach to microcracking and power-loss in photovoltaic modules. *Composite Structures*, 95:630–638, 2013.

[44] J Reinoso, M Paggi, and A Blázquez. A nonlinear finite thickness cohesive interface element for modeling delamination in fibre-reinforced composite laminates. *Composites Part B: Engineering*, 109:116–128, 2017.

[45] M Bischoff and E Ramm. Shear deformable shell elements for large strains and rotations. *International Journal for Numerical Methods in Engineering*, 40(23):4427–4449, 1997.

[46] S Klinkel and W Wagner. A geometrical non-linear brick element based on the eas-method. *International Journal for Numerical Methods in Engineering*, 40(24):4529–4545, 1997.

[47] M-A Msekh, J-M Sargado, M Jamshidian, PM Areias, and T Rabczuk. Abaqus implementation of phase-field model for brittle fracture. *Computational Materials Science*, 96:472–484, 2015.

[48] CV Verhoosel and R Borst. A phase-field model for cohesive fracture. *International Journal for numerical methods in Engineering*, 96(1):43–62, 2013.

[49] A-A Griffith. The phenomena of rupture and flow in solids. *Philosophical transactions of the royal society of london. Series A, containing papers of a mathematical or physical character*, 221:163–198, 1921.

[50] JC Simo and F Armero. Geometrically non-linear enhanced strain mixed methods and the method of incompatible modes. *International Journal for Numerical Methods in Engineering*, 33(7):1413–1449, 1992.

[51] M Paggi and P Wriggers. A nonlocal cohesive zone model for finite thickness interfaces–part i: mathematical formulation and validation with molecular dynamics. *Computational Materials Science*, 50(5):1625–1633, 2011.

[52] M Paggi and P Wriggers. A nonlocal cohesive zone model for finite thickness interfaces–part ii: Fe implementation and application to polycrystalline materials. *Computational Materials Science*, 50(5):1634–1643, 2011.

[53] J Reinoso and M Paggi. A consistent interface element formulation for geometrical and material nonlinearities. *Computational Mechanics*, 54(6):1569–1581, 2014.

[54] Francesco Parrinello, Guido Borino, and Roberto Caserta. Effective reference and current integration for large displacement interface. *GIMC-GMA Conference*, 2016.

[55] M Paggi and J Reinoso. An anisotropic large displacement cohesive zone model for fibrillar and crazing interfaces. *International Journal of Solids and Structures*, 69:106–120, 2015.

[56] V Mantič, L Távara, A Blázquez, E Graciani, and F París. A linear elastic-brittle interface model: application for the onset and propagation of a fibre-matrix interface crack under biaxial transverse loads. *International Journal of Fracture*, 195(1-2):15–38, 2015.

[57] L Távara, J Reinoso, D Castillo, and V Mantič. Mixed-mode failure of interfaces studied by the 2d linear elastic-brittle interface model: macro-and micro-mechanical finite element applications in composites. *The Journal of Adhesion*, (just-accepted), 2017.

[58] L Vu-Quoc and XG Tan. Optimal solid shells for non-linear analyses of multilayer composites. i. statics. *Computer Methods in Applied Mechanics and Engineering*, 192(9–10):975 – 1016, 2003.

[59] C Miehe. A theoretical and computational model for isotropic elastoplastic stress analysis in shells at large strains.

23

Computer Methods in Applied Mechanics and Engineering, 155(3-4):193–233, 1998.

[60] K Rah, WV Paepegem, AM Habraken, J Degrieck, RJA de Sousa, and RAF Valente. Optimal low-order fully integrated solid-shell elements. *Computational Mechanics*, 51(3):309–326, 2013.

[61] S Klinkel, F Gruttmann, and W Wagner. A continuum based three-dimensional shell element for laminated structures. *Computers & Structures*, 71(1):43–62, 1999.

[62] OC Zienkiewicz and RL Taylor. *The finite element method: solid mechanics*, volume 2. Butterworth-heinemann, 2000.

[63] Woong Lee, Yo-Han Yoo, and Hyunho Shin. Reconsideration of crack deflection at planar interfaces in layered systems. *Composites Science and Technology*, 64(15):2415 – 2423, 2004.

[64] Martin Sander, Sascha Dietrich, Matthias Pander, Matthias Ebert, and Jörg Bagdahn. Systematic investigation of cracks in encapsulated solar cells after mechanical loading. *Solar Energy Materials and Solar Cells*, 111:82–89, 2013.

[65] Marco Paggi, Sarah Kajari-Schröder, and Ulrich Eitner. Thermomechanical deformations in photovoltaic laminates. *The Journal of Strain Analysis for Engineering Design*, 46(8):772–782, 2011.